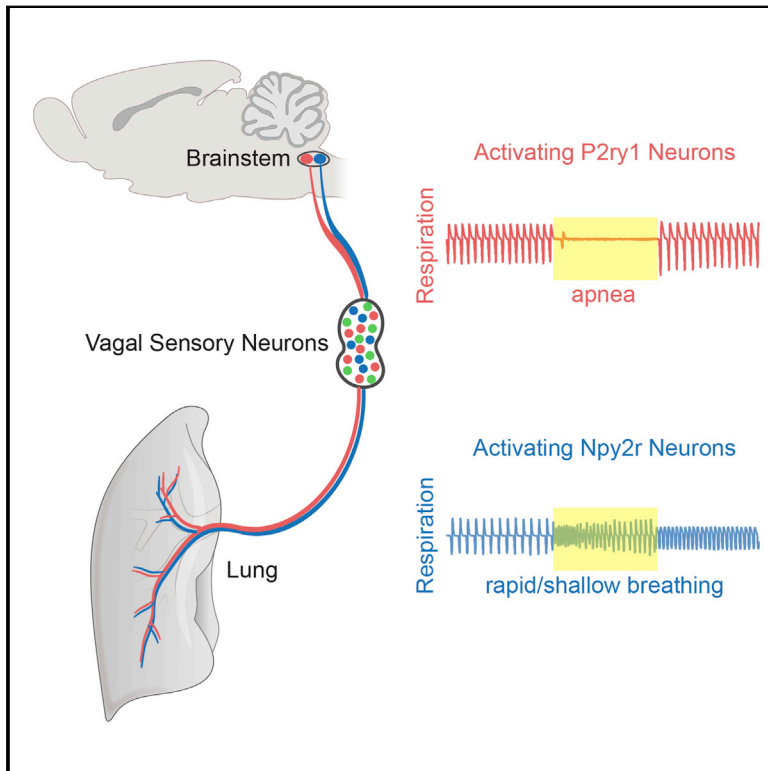Article

Vagal Sensory Neuron Subtypes that Differentially Control Breathing

Graphical Abstract

Authors

Rui B. Chang, David E. Strochlic, ...,
Benjamin D. Umans, Stephen D. Liberles

Correspondence

stephen_liberles@hms.harvard.edu

In Brief

Genetic control of vagal sensory neurons revealed two subtypes with distinct lung-to-brain connectivity. Optogenetic activation reveals that one class can acutely silence breathing, while the other can cause rapid, shallow breathing.

Highlights

- Genetic tools deconstruct the vagus nerve into several co-fasciculating labeled lines

- Two vagal sensory neuron types evoke powerful and distinct effects on breathing

- P2ry1 and Npy2r neurons differentially innervate the lung and brainstem

- P2ry1 neurons trap breathing in exhalation and do not impact heart rate

CellPress

Vagal Sensory Neuron Subtypes that Differentially Control Breathing

Rui B. Chang,[1,2] David E. Strochlic,[1,2] Erika K. Williams,[1] Benjamin D. Umans,[1] and Stephen D. Liberles[1,*]
[1]Department of Cell Biology, Harvard Medical School, Boston, MA 02115, USA
[2]Co-first author
*Correspondence: stephen_liberles@hms.harvard.edu
http://dx.doi.org/10.1016/j.cell.2015.03.022

SUMMARY

Breathing is essential for survival and under precise neural control. The vagus nerve is a major conduit between lung and brain required for normal respiration. Here, we identify two populations of mouse vagus nerve afferents (P2ry1, Npy2r), each a few hundred neurons, that exert powerful and opposing effects on breathing. Genetically guided anatomical mapping revealed that these neurons densely innervate the lung and send long-range projections to different brainstem targets. Npy2r neurons are largely slow-conducting C fibers, while P2ry1 neurons are largely fast-conducting A fibers that contact pulmonary endocrine cells (neuroepithelial bodies). Optogenetic stimulation of P2ry1 neurons acutely silences respiration, trapping animals in exhalation, while stimulating Npy2r neurons causes rapid, shallow breathing. Activating P2ry1 neurons did not impact heart rate or gastric pressure, other autonomic functions under vagal control. Thus, the vagus nerve contains intermingled sensory neurons constituting genetically definable labeled lines with different anatomical connections and physiological roles.

INTRODUCTION

Breathing is tightly regulated by the nervous system to ensure appropriate tissue oxygenation. Several classes of central and peripheral sensory neurons acutely regulate the respiratory cycle in response to changes in blood pH and gas composition, as well as external environment (Carr and Undem, 2003; Gonzalez et al., 1994; Guyenet et al., 2010). Among these, sensory neurons of the vagus nerve are the major source of nerve fibers that innervate the lung and airways, and are important for normal breathing. The vagus nerve contains sensory neurons that provide critical information needed to control respiration rate, regulate airway tone and defense, and in some species, evoke cough (Canning et al., 2006; Carr and Undem, 2003; Coleridge and Coleridge, 2011; Tränkner et al., 2014; Widdicombe, 2001). However, the diversity of lung-innervating sensory neurons remains poorly characterized at a molecular level, with specific neuron types that promote or restrict respiration genetically undefined.

The vagus nerve is the tenth cranial nerve, characterized by a wandering trajectory that provides extensive innervation of the neck, chest, and abdomen (Berthoud and Neuhuber, 2000). The vagus nerve controls not only respiration, but also basic physiological functions of the cardiovascular, immune, and digestive systems. Most vagal neurons (∼80%) provide ascending sensory information (Foley and DuBois, 1937), receiving input from thoracic tissues like heart and lung, and abdominal tissues like stomach and intestine. Electrophysiological studies revealed both chemosensory and mechanosensory neurons of the vagus nerve (Berthoud and Neuhuber, 2000; Paintal, 1973). Within the airways, vagal sensory neurons detect irritants, cues associated with inflammation and illness, and mechanical stretch of the lung during cycles of inhalation and exhalation (Carr and Undem, 2003; Paintal, 1973; Widdicombe, 2001). The cell bodies of sensory fibers reside in pairs of ganglia at the base of the skull, including the adjacent nodose and jugular ganglia (the nodose/jugular complex). Afferent vagal axons enter the brain bilaterally through the jugular foramina and primarily target the nucleus of the solitary tract (NTS), a brainstem nucleus that transmits sensory information to deeper brain structures and descending motor nuclei (Berthoud and Neuhuber, 2000; Kubin et al., 2006).

We reasoned that the vagus nerve likely contains a diversity of molecularly distinct neuron types with different anatomical projections and functions. Previous descriptive classifications of vagal sensory neurons were based on neuron response properties like conduction velocity and adaptation rate (Carr and Undem, 2003) and did not enable genetic control for specific analysis. Furthermore, classical procedures to manipulate vagus nerve function—surgical vagotomy and implantation of electrical stimulators—impact many neuron types in both the motor and sensory arms (Groves and Brown, 2005; Schachter and Saper, 1998). These procedures implicate the vagus nerve in many physiological systems and offer therapeutic options for several otherwise intractable diseases (Groves and Brown, 2005; Schachter and Saper, 1998). However, because they lack cell specificity, they are blunt tools for analytical studies and cause unwanted side effects in patients. Gaining genetic access to the diversity of vagal sensory neurons might help disentangle the neural control of autonomic physiology. Here, we used a molecular and genetic approach to reveal the identity of two populations of breathing-control neurons in the vagus nerve.
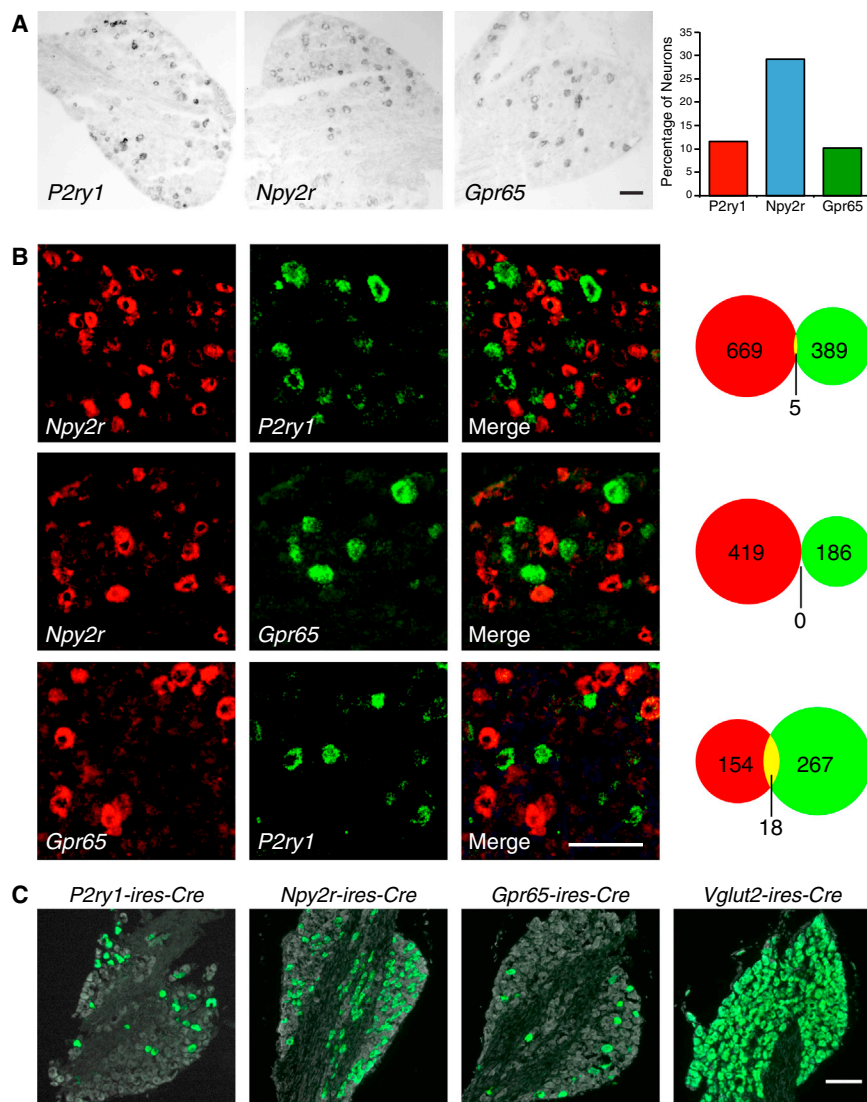
Figure 1. Genetic Control of Sensory Neuron Types in the Vagus Nerve

(A) RNA in situ hybridization experiments in the nodose/jugular complex revealed that *P2ry1*, *Npy2r*, and *Gpr65* are expressed in subsets of vagal sensory neurons.

(B) Two color in situ hybridization experiments for indicated genes revealed largely non-overlapping neuron populations. The numbers of cells expressing one receptor (red or green) or both receptors (yellow) were counted.

(C) The indicated Cre lines were crossed with *lox-L10-GFP* mice, and in offspring, fixed cryosections of the nodose/jugular complex were imaged by fluorescence microscopy. Native GFP fluorescence (green) and a fluorescent Nissl stain (gray) were visualized. Scale bars, 100 μm. See also Figures S1 and S2.

2001); *Gpr65* is expressed in 10.2% of vagal sensory neurons (126/1,237, ~230 neurons per ganglia complex), *P2ry1* is expressed in 11.6% of vagal sensory neurons (190/1,631, ~280 neurons per ganglia complex), and *Npy2r* is expressed in 29.2% of vagal sensory neurons (445/1,524, ~670 neurons per ganglia complex). Vagal NPY2R was proposed, and debated, to function in nutrient-evoked satiety (Karra and Batterham, 2010), while roles for vagal P2RY1 and GPR65 were not previously reported.

Two color in situ hybridization analysis in the nodose/jugular complex revealed that *Npy2r*, *P2ry1*, and *Gpr65* were predominantly expressed in different vagal sensory neurons (Figure 1B). Most Npy2r neurons did not express *P2ry1* (99%, 669/674) or *Gpr65* (100%, 419/419); most P2ry1 neurons did not express *Gpr65* (94%, 267/285) or *Npy2r* (99%, 389/394); and most Gpr65 neurons did not express *P2ry1* (90%, 154/172) or *Npy2r* (100%, 186/186). Thus, three major classes of vagal afferents are distinguishable by genetic markers and together account for ~50%–60% of nodose/jugular sensory neurons.

RESULTS

Identifying Cell Surface Receptors of the Sensory Vagus Nerve

Molecularly distinct neuron subtypes have been classified within several sensory systems (Abraira and Ginty, 2013; Basbaum et al., 2009; Dong et al., 2001; Munger et al., 2009; Yarmolinsky et al., 2009). To identify markers for subtypes of vagal afferents, we used a genome-based strategy that previously enabled identification of families of olfactory receptors (Liberles and Buck, 2006; Liberles et al., 2009). Expression levels of ~400 G protein-coupled receptors (GPCRs) were quantified in nodose/jugular complex cDNA by qPCR. Candidate genes were cloned for cRNA riboprobe synthesis and examined for expression in neuronal subsets by in situ hybridization. These experiments revealed three GPCR genes, *P2ry1*, *Npy2r*, and *Gpr65*, to be expressed in subsets of vagus nerve afferents (Figure 1A). Each nodose/jugular complex contains ~2,300 neurons (Fox et al.,
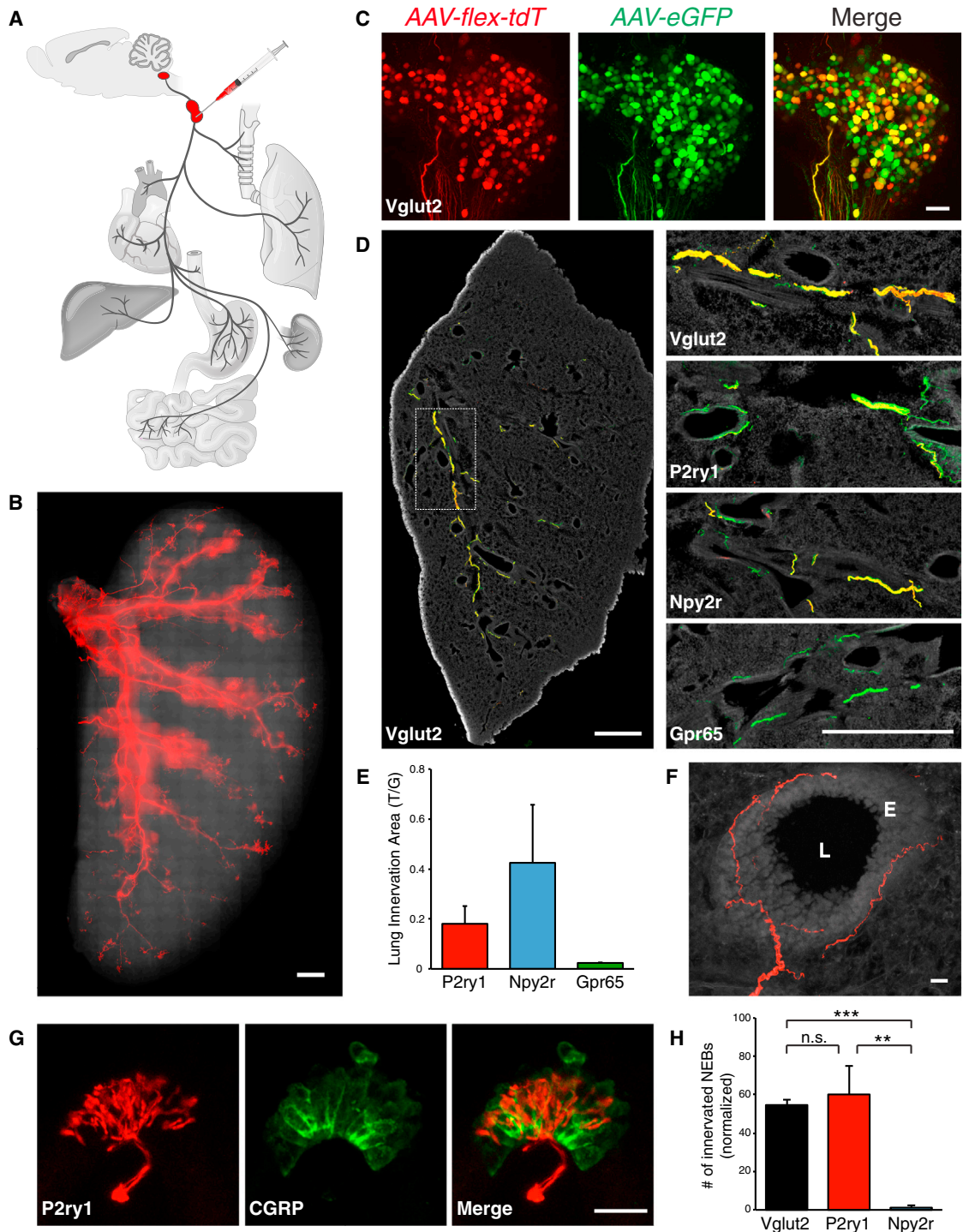
Genetic Control of Vagus Nerve Sensory Neurons

Cre/LoxP technology enables powerful, genetically guided approaches for connectivity mapping and remote control of neural activity (Rogan and Roth, 2011). We generated *P2ry1-ires-Cre*, *Gpr65-ires-Cre*, and *Npy2r-ires-Cre* knockin mice (Figure S1), in which Cre recombinase is co-transcribed with the receptor gene and independently translated from an internal ribosome entry site (IRES) sequence (Kim et al., 1992). Each Cre knockin line was crossed with reporter mice harboring a Cre-dependent *L10-GFP* allele (*lox-L10-GFP*; similar reporter alleles are herein referred to as *lox-reporter*) (Krashes et al., 2014), and in offspring,

Figure 2. Visualizing Vagal Afferents in the Lung

(A) Cartoon depiction of the neural tracing strategy, which involved infection of a Cre-dependent AAV (*AAV-flex-tdTomato*) and/or a Cre-independent AAV (*AAV-eGFP*) in the nodose/jugular complex of *ires-Cre* knockin mice.

(B) Whole-mount analysis of native tdTomato fluorescence in a flattened lung lobe from a *Vglut2-ires-Cre* mouse infected with *AAV-flex-tdTomato*. Scale bar, 1 mM.

(C) Whole-mount analysis (maximum projection of stacked confocal images) of native tdTomato (tdT) and GFP fluorescence in the nodose/jugular complex of a *Vglut2-ires-Cre* mouse infected with *AAV-flex-tdTomato* and *AAV-eGFP*. Scale bar, 100 μm.

(D) Different *ires-Cre* lines were infected with *AAV-flex-tdTomato* and *AAV-eGFP*, and fibers were visualized in fixed lung cryosections by immunohistochemistry for tdTomato (red) and GFP (green). Scale bars, 1 mm.

(legend continued on next page)

subsets of vagal sensory neurons displayed bright, native GFP fluorescence (Figure 1C). Cre recombinase drives reporter expression to appropriate neurons of the nodose/jugular complex, as determined by two color in situ hybridization analysis (Figure S1). In sum, 94% of P2ry1 neurons express reporter in *P2ry1-ires-Cre*; *lox-Channelrhodopsin2-eYFP* mice, 94% of Npy2r neurons express reporter in *Npy2r-ires-Cre*; *lox-Channelrhodopsin2-eYFP* mice, and 88% of Gpr65 neurons express reporter in *Gpr65-ires-Cre*; *lox-tdTomato* mice. In contrast, 3.0% of Npy2r neurons and 2.4% of Gpr65 neurons express reporter in *P2ry1-ires-Cre*; *lox-Channelrhodopsin2-eYFP* mice. As is commonly observed using *Cre/LoxP* techniques, we detected some reporter positive, receptor negative neurons (19%–27%), which could be due to imperfect detection of receptor expression by in situ hybridization techniques or transient expression of Cre recombinase during development (Schmidt-Supprian and Rajewsky, 2007).

In addition, we obtained *Vglut2-ires-Cre* and *Chat-ires-Cre* mice (Rossi et al., 2011; Vong et al., 2011), which provided important tools for global control of sensory neurons and motor neurons respectively. Calcium imaging experiments in acute neuron cultures from the nodose/jugular complex of *Vglut2-ires-Cre*; *lox-tdTomato* mice revealed that 100% (168/168) of KCl-responsive sensory neurons expressed tdTomato. Furthermore, in *Vglut2-ires-Cre*; *lox-L10-GFP* mice, GFP was expressed in 99.4% (632/636) of sensory neurons, but only rare motor neurons (6/845 dorsal motor nucleus of the vagus or DMV neurons and 28/320 nucleus ambiguus neurons) (Figure S2). We also obtained *Chat-ires-Cre* mice that drive reporter expression in most motor neurons (376/442 DMV neurons and 84/123 nucleus ambiguus neurons), but not in sensory neurons (0/599). In triple transgenic *Vglut2-ires-Cre*; *lox-tdTomato*; *Chat-GFP* mice, motor and sensory fibers are differentially visualized and partially segregated within the vagus nerve trunk (Figure S2). Together, this toolbox of Cre lines enables differential genetic access to the vagus nerve motor and sensory arms, as well as three molecularly distinct sensory neuron subpopulations.

Visualizing Lung-to-Brain Sensory Neurons of the Vagus Nerve

We asked whether any of these genetically defined vagal afferents innervated the lung and thus might control breathing. The peripheral projections of Cre-expressing sensory neurons were traced using fluorescent reporters introduced by adeno-associated virus (AAV) infection of the nodose/jugular complex (Figure 2A). Since each *ires-Cre* line drives reporter expression in locations other than the nodose/jugular complex, AAV infections ensured that fluorescent afferents were specifically derived from the sensory vagus nerve. Infection efficiency was assessed by injection of *Vglut2-ires-Cre*; *lox-L10-GFP* mice with an AAV con-

taining a Cre-dependent *tdTomato* allele (*AAV-flex-tdTomato*). At 4 weeks after infection, tdTomato fluorescence was observed in ~45% of GFP-containing neuronal cell bodies (Figure S3) and was sufficiently bright to detect by whole mount analysis of the nodose/jugular complex and nerve trunk. Cre-expressing cells were similarly infected in *P2ry1-ires-Cre*, *Npy2r-ires-Cre*, and *Gpr65-ires-Cre* mice (Figure S3). Red fluorescence was not observed in uninfected Cre mice or in wild-type mice infected with *AAV-flex-tdTomato* (Figure S3).

Infection of *Vglut2-ires-Cre* mice with *AAV-flex-tdTomato* yielded bright red fibers throughout the lungs and airways that could be readily visualized by whole mount analysis of a flattened lung lobe (Figure 2B). A dual infection strategy was used to quantify airway innervation by vagal afferent populations labeled in different Cre lines (Figures 2C and 2D). The nodose/jugular complex was simultaneously infected with *AAV-flex-tdTomato* and a second AAV containing a Cre-independent *GFP* allele for normalization (*AAV-eGFP*). Dual immunohistochemistry for GFP and tdTomato was performed on lung cryosections obtained 4 weeks after infection. The areas of tdTomato- and GFP-derived fluorescence were measured in a 17.5-mm^2 lung region containing several principal airways, and the ratio of tdTomato/GFP (T/G) labeling calculated. Dual virus infection experiments in *Vglut2-ires-Cre* mice yielded GFP- and tdTomato-containing fibers that were highly co-localized throughout the lung and a benchmark T/G fluorescence ratio of 0.79. Related experiments using other Cre lines (Figure 2E) revealed that Npy2r and P2ry1 neurons provided dense innervation of the lung (0.42 T/G and 0.18 T/G respectively, or 54% and 23% of T/G observed in *Vglut2-ires-Cre* mice), while Gpr65 neurons did not (0.02 T/G, 3%). Npy2r and P2ry1 neurons account for the majority of lung-innervating vagal fibers, but not all. Furthermore, Npy2r and P2ry1 neurons do not exclusively innervate the airways, as labeled fibers were also detected in the heart and stomach. It is possible that each neuron type performs a similar sensory function in multiple tissues (such as detecting organ stretch or inflammation), and/or that additional markers are needed to subdivide these neuron classes further.
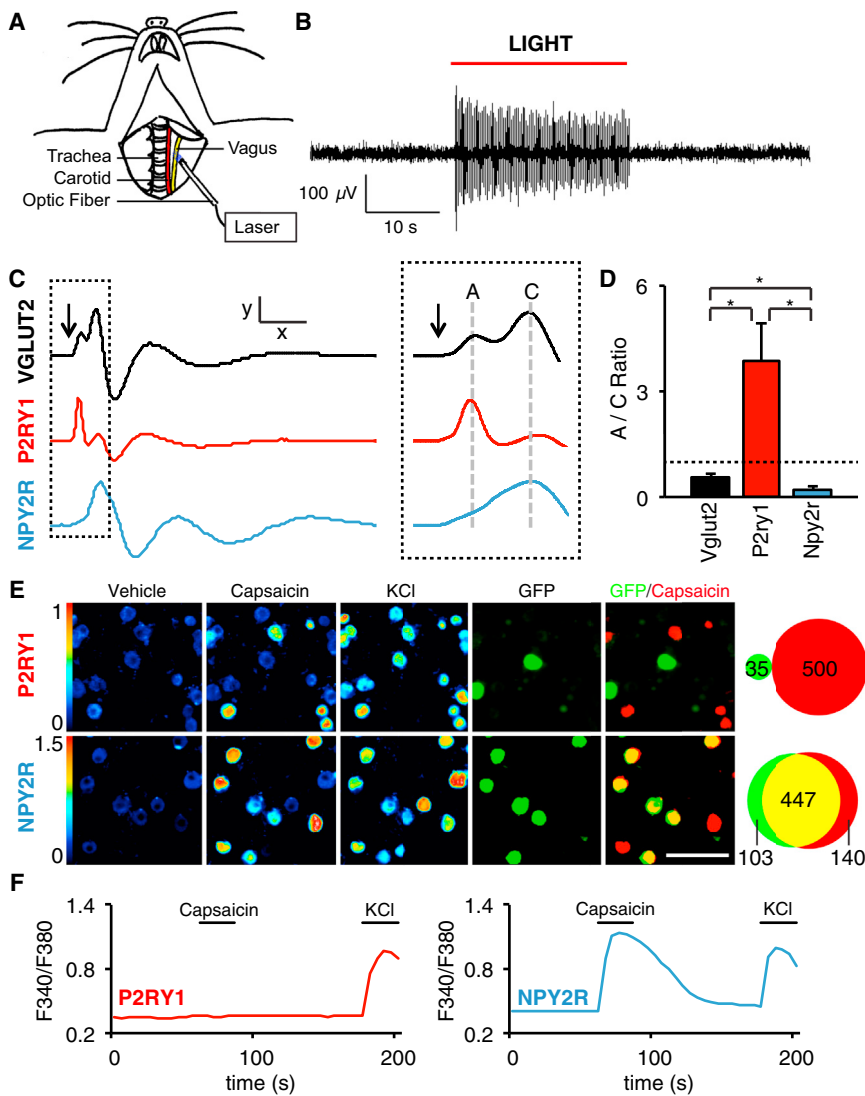
Within the lung, sensory fibers visualized in *P2ry1-ires-Cre* and *Npy2r-ires-Cre* mice displayed different arborization patterns and terminal morphologies. In both lines, the majority of fibers coursed along the major airways beneath and parallel to the smooth muscle layer (Figure 2F). P2ry1 neurons, but not Npy2r neurons, formed stereotyped candelabra endings at neuroepithelial bodies, clusters of pulmonary secretory cells embedded within the epithelium and revealed by calcitonin gene-related peptide (CGRP) immunoreactivity (Figure 2G) (Brouns et al., 2009). P2ry1 neurons account for most or all vagal innervation of neuroepithelial bodies, based on the frequency of tdTomato-positive fibers in *Vglut2-ires-Cre* and *P2ry1-ires-Cre* mice (Figure 2H). Vagal afferents visualized in

(E) Quantitative analysis of lung innervation in 17.5-mm^2 lung regions expressed as an area ratio of T/G-derived immunofluorescence (mean ± SEM, see Results and Extended Experimental Procedures for additional detail on T/G calculation).

(F) High resolution image of a representative vagal afferent beneath the epithelial layer, (E), of a major airway (airway lumen, L). Scale bar, 20 μm.

(G) Representative P2ry1 candelabra terminal (tdT fluorescence) at a neuroepithelial body (CGRP immunostaining, green). Scale bar, 20 μm.

(H) The number of neuroepithelial bodies (NEBs) innervated by each neuron type after visualization with *AAV-flex-tdTomato* and normalization with *AAV-eGFP* (n = 3–5, mean ± SEM, **p < 0.01, and ***p < 0.001). See also Figure S3.

Figure 3. Characterization of Vagal P2ry1 and Npy2r Neurons

(A) Cartoon depiction of optogenetic strategy. The vagus nerve is surgically exposed in anesthetized mice and illuminated to activate ChR2-expressing sensory neurons.

(B) Whole nerve electrophysiological recordings in *Vglut2-ChR2* mice revealed light-induced action potentials.

(C) Compound action potentials following brief optogenetic stimulation (arrow) in *Vglut2-ChR2*, *P2ry1-ChR2*, and *Npy2r-ChR2* mice. A and C fibers were classified based on conduction velocity (Figure S4) x = 5 ms, y = 110 μV (Vglut2), 62 μV (P2ry1), 160 μV (Npy2r), and dashed inset, x = 1.45 ms.

(D) The ratio of A to C fibers was calculated by integrating corresponding peak area in the compound action potential; dashed line: A/C ration of 1 (n = 5–8, mean ± SEM, and *p < 0.05).

(E) Calcium imaging of single neuron responses to capsaicin (2 μM) and KCl (50 mM) in acute ganglia cultures from *P2ry1-ires-Cre*; *lox-L10-GFP* and *Npy2r-ires-Cre*; *lox-L10-GFP* mice. (Left panels, color scale = 340/380 nm Fura-2 excitation ratio and right panels, neurons expressing GFP [green, native fluorescence] and responding to capsaicin [red] are superimposed and counted). Scale bar, 100 μm.

(F) Representative traces for single neurons imaged in (E). See also Figure S4.

that were not similarly observed in control animals lacking Cre recombinase (Figure 3B).

Brief optogenetic stimulation (0.8 ms) of all sensory neurons in *Vglut2-ChR2* mice generated a compound action potential resulting from summation of slow-conducting and fast-conducting neurons (Figure 3C). Propagation speed was calculated by varying the distance between the optic fiber and recording electrodes (Figure S4), and two major peaks were resolved with conduction velocities characteristic of A fibers (10.2 ± 4.0 m/s) and C fibers (0.71 ± 0.04 m/s). Similar experiments in *P2ry1-ChR2* and *Npy2r-ChR2* mice revealed that most P2ry1 neurons were A fibers and most Npy2r neurons were C fibers (Figure 3D).

Sensory afferents in the lung are also heterogeneous with respect to capsaicin sensitivity, with most C fibers being capsaicin-responsive. Acute cultures of nodose/jugular ganglia were prepared from *P2ry1-ires-Cre*; *lox-L10-GFP* and *Npy2r-ires-Cre*; *lox-L10-GFP* mice and responses of single, genetically defined neurons were measured by calcium imaging with Fura-2. Capsaicin activated 60.7% (1,087/1,791) of all vagal sensory neurons, 0% (0/35) of P2ry1 neurons, and 81.3% (447/550) of Npy2r neurons (Figures 3E and 3F). Furthermore, two color in situ hybridization analysis revealed that most Npy2r (62%, 193/310) neurons expressed the gene encoding the capsaicin receptor TRPV1, while most P2ry1 neurons (95%, 213/224) did
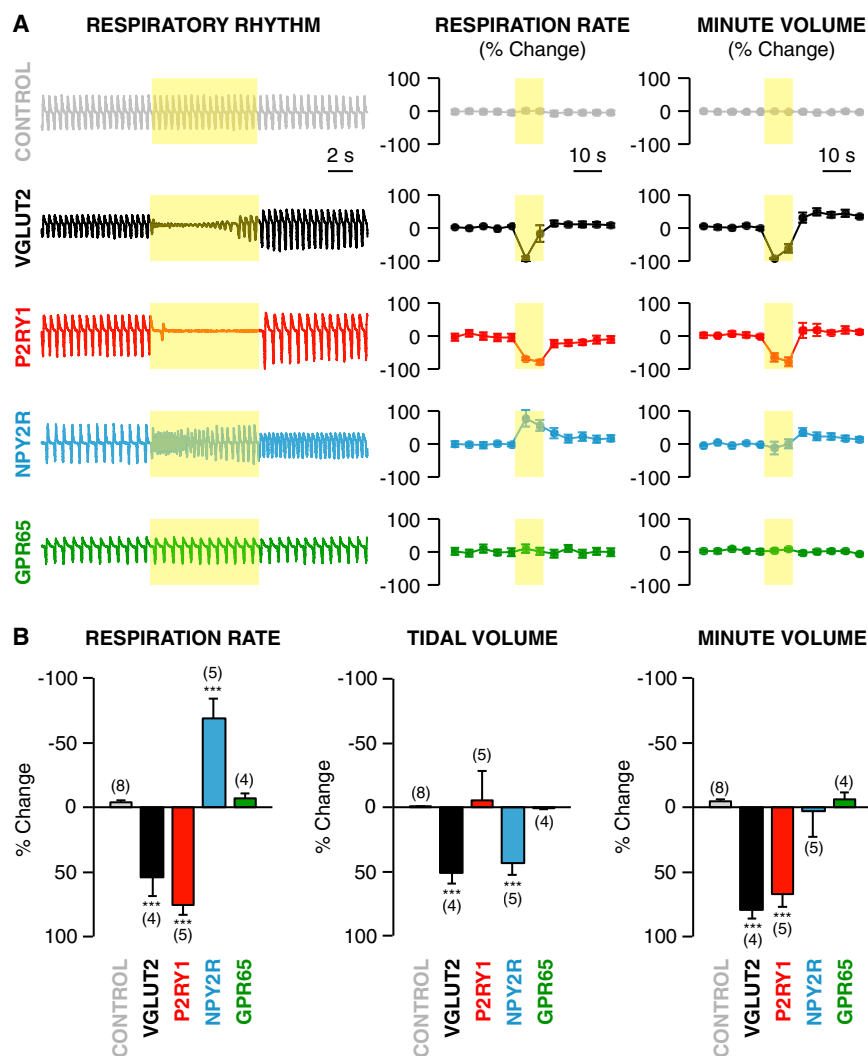
Npy2r-ires-Cre mice did not innervate neuroepithelial bodies, but were instead enriched near alveoli in the lung respiratory zone (Figure S3).

Physiological and Molecular Characterization of Vagal P2ry1 and Npy2r Neurons

Vagal afferents in the lung are a heterogeneous group of fast-conducting myelinated A fibers and slow-conducting unmyelinated C fibers (Carr and Undem, 2003). We used a channelrhodopsin-assisted approach to measure the specific conduction velocities of vagal P2ry1 and Npy2r neurons. We independently crossed wild-type, *Vglut2-ires-Cre*, *P2ry1-ires-Cre*, and *Npy2r-ires-Cre* mice with reporter mice containing a Cre-dependent *channelrhodopsin-2 (ChR2)* allele (*lox-Channelrhodopsin2-eYFP*, offspring of each cross are subsequently referred to as *driver-ChR2* or, in controls, *lox-ChR2* mice). Optogenetic activation of vagal fibers was achieved in anesthetized animals by focal illumination of the vagus nerve trunk (Figure 3A). Whole nerve recordings revealed robust light-induced action potentials

Figure 4. Remote Control of Breathing

(A) Respiratory effects following focal vagus nerve illumination (yellow shading) in *lox-ChR2*, *Vglut2-ChR2*, *P2ry1-ChR2*, *Npy2r-ChR2*, and *Gpr65-ChR2* mice. Respiratory rhythms (representative traces) were measured using a pressure transducer via trachea cannula. Changes in respiration rate and minute volume were calculated over time, with each data point reflecting a 5 s bin.

(B) Light-induced changes in respiration rate, tidal volume, and minute volume were calculated over the 10 s trial (n = 4–8 as indicated, mean ± SEM, and ***$p < 0.001$). See also Figures S5 and S6.

tion (Figure 4). In each animal tested, illumination caused an abrupt pause in breathing that persisted for an average of 6.2 s, followed by a secondary phase characterized by shallow breathing until the light was turned off. Over the 10 s trial, light-induced activation of vagal sensory neurons caused a 54% decrease in respiration rate, a 52% decrease in tidal volume, and a 79% decrease in minute volume. In contrast, similar changes in respiration were not observed in *Chat-ChR2* or *lox-ChR2* mice (Figures 4 and S5). These findings are consistent with a pronounced role for vagal sensory neurons in breathing regulation via reflex circuitry involving descending spinal motor neurons.

Next, we asked if vagal subpopulations labeled in *P2ry1-ires-Cre*, *Gpr65-ires-Cre*, and *Npy2r-ires-Cre* mice elicited similar effects (Figure 4). Activation of P2ry1 neurons, which represent 11.6% of the vagal sensory neuron repertoire, caused an immediate and striking inhibition of respiration that was of statistically similar acute duration (7.9 s) to that observed in *Vglut2-ChR2* mice. However, the secondary phase involved full breaths that were rarer than those observed during activation of all vagal afferents in *Vglut2-ChR2* mice (Figure S6). Over the 10 s trial, activating P2ry1 neurons caused a 72% decrease in respiration rate, no significant effect on tidal volume (5.5% increase), and a 67% decrease in minute volume. The different respiratory effects observed following light stimulation in *P2ry1-ChR2* and *Vglut2-ChR2* mice suggested contributions from other vagal sensory neurons in breathing control.

Activating Npy2r neurons evoked a different respiratory response characterized by rapid and shallow breathing. In *Npy2r-ChR2* mice, we observed a light-induced 68% increase in respiration rate, a 44% decrease in tidal volume, and a 3% decrease in minute volume. Light-induced respiratory effects in *P2ry1-ires-Cre* and *Npy2r-ires-Cre* mice are seemingly due to stimulation of different sensory neuron populations; contributions from motor fibers are unlikely since bulk activation of motor neurons in *Chat-ires-Cre* mice had no effect on respiration rate,
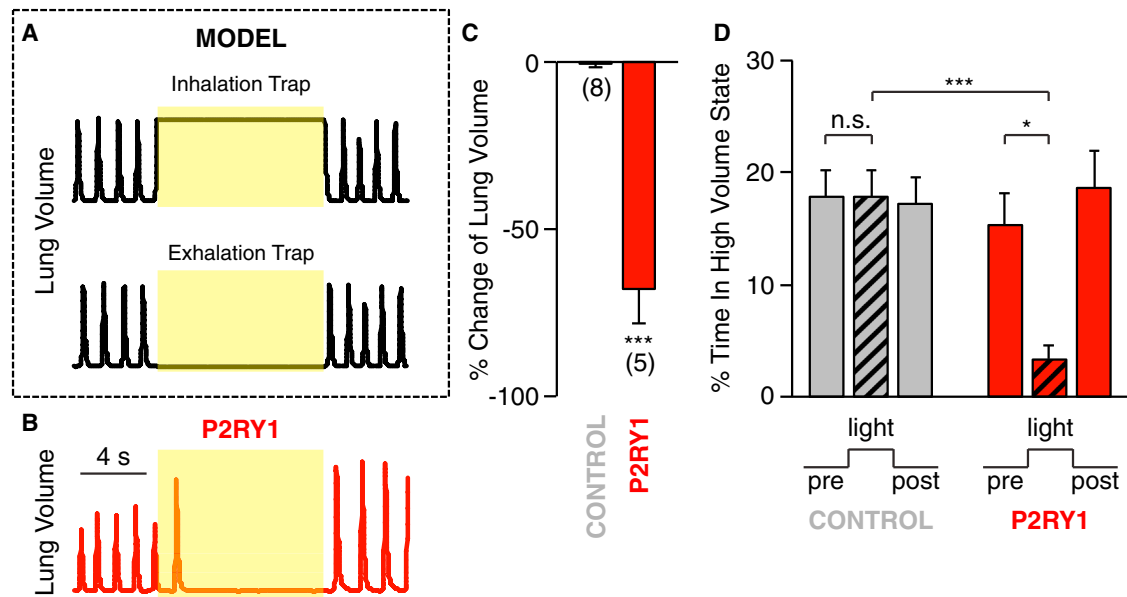
not (Figure S4). For comparison, the mechanoreceptor Piezo2 (Coste et al., 2010) was instead co-expressed in many P2ry1 neurons (44%, 170/388), rare Npy2r neurons (4.7%, 14/297), and not in Gpr65 neurons (0%, 0/94) (Figure S4). Taken together, P2ry1 neurons are mostly fast-conducting, capsaicin-insensitive A fibers, while Npy2r neurons are mostly slow-conducting, capsaicin-responsive C fibers.

Optogenetic Control of the Respiratory Cycle

We reasoned that lung-innervating sensory neurons labeled in *P2ry1-ires-Cre* and *Npy2r-ires-Cre* mice might control breathing. Classical techniques to study vagus nerve functions—surgical vagotomy and bulk electrical stimulation—are unable to distinguish the specific contributions of different co-fasciculating fibers. Here, we used optogenetic approaches in freely breathing, anesthetized *lox-ChR2, Vglut2-ChR2, Chat-ChR2, P2ry1-ChR2, Gpr65-ChR2,* and *Npy2r-ChR2* mice to query the roles of particular vagal neuron populations in respiratory physiology.

Optogenetic activation of all vagal sensory neurons in *Vglut2-ChR2* mice revealed powerful light-induced changes in respira-

Figure 5. P2ry1 Neurons Trap Respiration in a State of Exhalation
(A) Theoretical models of lung volume changes during light-induced inhalation and exhalation trapping.
(B) Representative data showing changes in lung volume following optogenetic activation of vagal afferents in *P2ry1-ChR2* mice.
(C) Percentage change in total lung volume evoked by light in *P2ry1-ChR2* mice (n = 5) and control mice (*lox-ChR2*) (n = 8). Total lung volume was calculated by integrating lung volume across 10 s periods before and during light stimulation.
(D) The percentage of time *P2ry1-ChR2* mice and control mice were in a high lung volume state before, during, and after light stimulation. High volume state was defined as greater than mean volume during tidal breathing (mean ± SEM, *p < 0.05, and ***p < 0.001).

tidal volume, or minute volume (Figure S5). Likewise, activating Gpr65 neurons had no significant effect on these breathing parameters, and together with their sparse lung innervation, Gpr65 neurons likely mediate other vagus nerve functions. The different respiratory effects of Npy2r, P2ry1, and Gpr65 neurons, or lack thereof, suggest that the vagus nerve contains functionally segregated labeled lines within the context of the respiratory system.

P2ry1 neurons caused an acute pause in respiration that could be due to sustained inhalation (breath holding) or exhalation. These potential mechanisms could be distinguished by measuring light-induced changes in lung volume (Figure 5); animals trapped in inhalation would have increased lung volume, while animals trapped in exhalation would have decreased lung volume. We observed that light-induced activation of P2ry1 neurons decreased lung volume (68% decrease in integrated lung volume over the 10 s trial), consistent with exhalation trapping and decreased time spent with lungs in a high volume state (77% decrease, with high volume state defined as lung volume greater than mean lung volume during tidal breathing). Similar experiments in control animals lacking a Cre driver (*lox-ChR2*) failed to show a significant decrease in lung volume (0.6%) or time in a high volume state (0.4%).

Next, we asked whether P2ry1 and Npy2r neurons control other autonomic functions of the vagus nerve. We used optogenetic approaches to activate vagal sensory neurons in *lox-ChR2*, *Vglut2-ChR2*, *P2ry1-ChR2*, and *Npy2r-ChR2* mice, and measured heart rate by electrocardiogram (ECG) recordings and gastric pressure by a cannulated pressure sensor. Activating

all sensory neurons in *Vglut2-ChR2* mice caused a profound drop in heart rate (−85%) and a decrease in gastric pressure (−11.3%), with both tonic and phasic components affected. Specifically activating P2ry1 neurons, however, had no significant effect on heart rate (−3.8%) or gastric pressure (−2.2%) (Figure 6), while activating vagal Npy2r neurons decreased both heart rate (−41.2%) and gastric pressure (−12.8%) (Figure S5). It is possible that the *Npy2r-ires-Cre* allele drives reporter expression in multiple neuron subtypes with specific functions, or in a single neuron type that impacts multiple organ systems. Results with P2ry1 neurons indicate that vagal control of breathing can be dissociated from effects on heart rate and gastric pressure by acute and selective stimulation of particular sensory neurons.

Regionalization of Sensory Neuron Inputs in the Brainstem
The different respiratory effects evoked by P2ry1 and Npy2r sensory neurons suggest engagement of distinct higher-order neural circuits. The axons of vagal sensory neurons densely innervate the NTS, area postrema, and spinal trigeminal nucleus (Berthoud and Neuhuber, 2000; Kalia and Mesulam, 1980), and topographic organization of vagal inputs in the NTS based on either physiological function or organ innervation has been proposed (Altschuler et al., 1989; Bailey et al., 2006; Katz and Karten, 1983; Kubin et al., 2006), but debated (Andresen et al., 2012). Here, we used genetically encoded neural tracers to ask how inputs from P2ry1 and Npy2r neurons are organized centrally.

We used AAV-directed neural tracing technology to visualize axons of Cre-expressing vagal sensory neurons in the brainstem
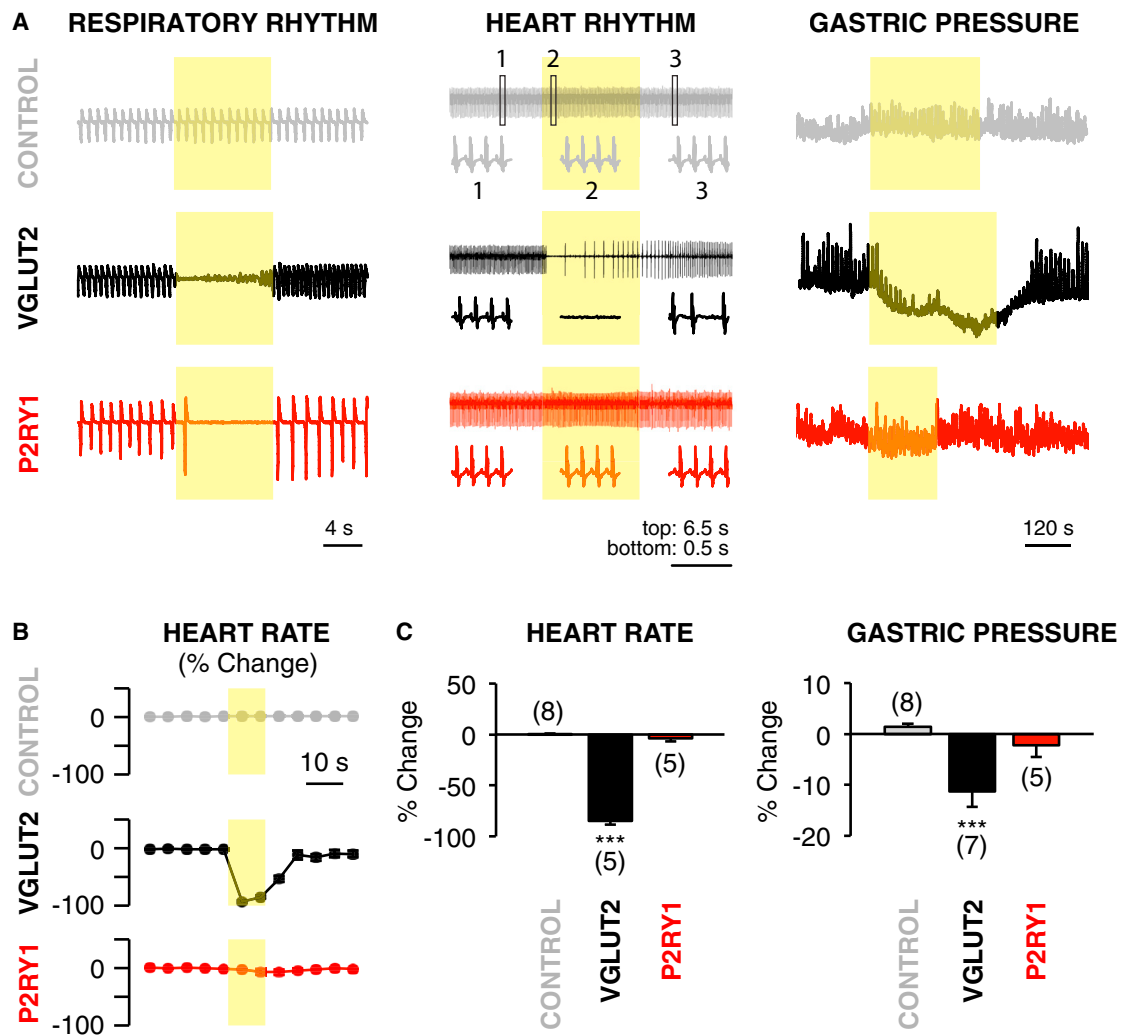
Figure 6. P2ry1 Neurons Acutely Control Breathing, but Not Gastric Pressure or Heart Rate

(A) Measurements (representative traces) of respiratory rhythm, heart rhythm, and gastric pressure following focal illumination (yellow shading) of the vagus nerve in anesthetized *P2ry1-ChR2*, *Vglut2-ChR2*, and control (*lox-ChR2*) mice. Heart rate was measured by ECG, with boxed insets showing rhythms before (1, left), during (2, middle), and after (3, right) light exposure. Intraluminal gastric pressure was measured using a pressure transducer inserted through the pyloric sphincter.

(B) Changes in heart rate (normalized from a 30 s pre-stimulus period) were calculated over time, with each data point reflecting a 5 s bin.

(C) Changes in heart rate and gastric pressure were calculated over the first 10 s or 3 min of light stimulation respectively (mean ± SEM and ***p < 0.001). See also Figure S5.

(Figures 7 and S7). We infected the nodose/jugular complex with both *AAV-flex-tdTomato* and *AAV-eGFP* for visualizing Cre-expressing neurons (red) in the context of all types of vagal sensory fibers (green). Dual infection of *Vglut2-ires-Cre* mice yielded red and green fibers penetrating the brain ipsilateral to the injection site and dense arborizations in both the NTS and area postrema. Arborizations occurred bilaterally in the NTS, with enrichment ipsilateral to the infected ganglia. Next, we performed similar experiments in *P2ry1-ires-Cre* mice and observed that the projection field of P2ry1 neurons was spatially confined and did not extend over the entire vagal NTS. Vagal P2ry1 neurons arborized immediately proximal to the ascending fiber tract in the lateral region of the NTS, and these lateral branches were observed throughout

the anterior-posterior axis. Intriguingly, the dorsal respiratory group, which contains second order neurons that control respiration, is located in the lateral NTS (Saether et al., 1987; Speck and Feldman, 1982). Similar experiments in *Npy2r-ires-Cre* mice revealed that Npy2r neurons instead innervated a different NTS region, with fibers predominantly emerging in the medial posterior aspects of the vagal NTS and area postrema, regions known to receive pulmonary C fiber input (Kubin et al., 1991, 2006). We quantified innervation density along the medial-lateral axis of the NTS and in the area postrema by calculating the area of red fibers and normalizing to the area of green fibers. We observed 21-fold higher levels of P2ry1 neuron-derived fluorescence compared with Npy2r neuron-derived fluorescence in laterally arborizing
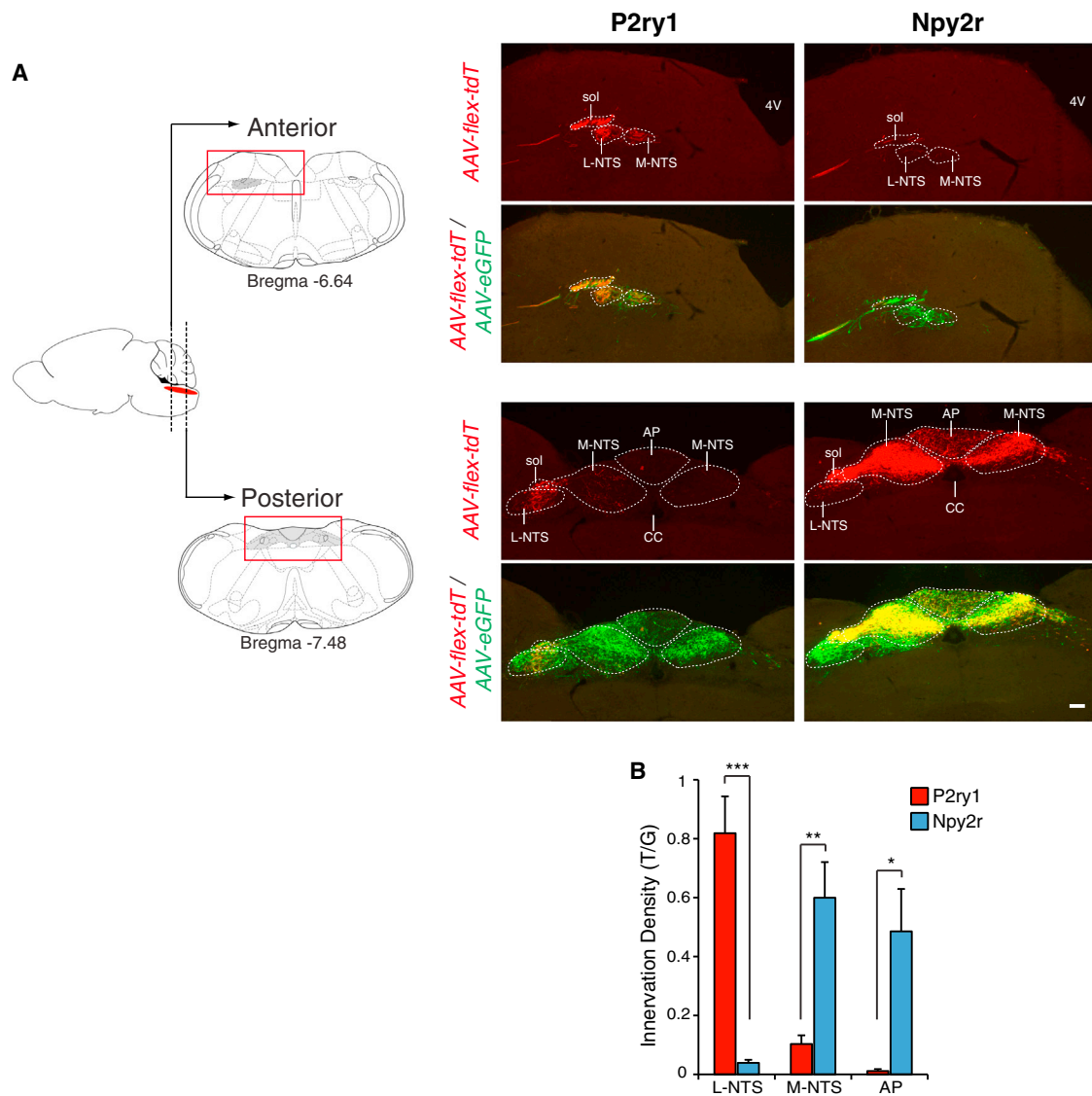
Figure 7. Non-Overlapping Central Projections of Vagal P2ry1 and Npy2r Neurons

(A) The nodose/jugular complex of *P2ry1-ires-Cre* and *Npy2r-ires-Cre* mice was infected with *AAV-flex-tdTomato* (*AAV-flex-tdT*) and *AAV-eGFP*. At 4 weeks after infection, fixed brainstem cryosections were analyzed by two color immunohistochemistry for tdTomato (red) and eGFP (green). Representative images of anterior and posterior brainstem containing the vagal projection field are shown (full rostral-caudal series, Figure S7). Solitary tract, sol; fourth ventricle, 4V; central canal, CC; area postrema, AP; L-NTS includes ventral, lateral, ventrolateral, interstitial, and intermediate NTS subnuclei; and M-NTS includes dorsolateral, dorsomedial, medial, and commisural NTS subnuclei. Scale bar, 100 μm.

(B) Quantitative analysis of innervation by P2ry1 and Npy2r fibers in L-NTS, M-NTS, and AP, expressed as an area ratio of T/G fluorescence. Fluorescence was summed in every eighth section (25 μm) from Bregma −6.4 mm to −7.8 mm. (n = 4, mean ± SEM, *p < 0.05, **p < 0.01, and ***p < 0.001). See also Figure S7.

NTS fibers. In contrast, we observed 6-fold and 43-fold higher levels of Npy2r neuron-derived fluorescence compared with P2ry1 neuron-derived fluorescence in medially arborizing NTS fibers and the area postrema, respectively. Thus, we observed non-overlapping and highly regionalized central projections of P2ry1 and Npy2r neurons that involved innervation of different NTS subnuclei. Together, these findings suggest that P2ry1 and Npy2r neurons engage different higher order neural circuits and are consistent with a brainstem map of vagal inputs that is at least partially linked to physiological function.

DISCUSSION

The vagus nerve provides the major sensory innervation of the lung and mediates basic physiological functions in breathing control and respiratory defense. Understanding the diversity of lung-innervating sensory neurons is an essential step toward disentangling the neural control of respiration.

Lung-innervating sensory neurons have been distinguished by their response kinetics and adaptation rates (Carr and Undem, 2003). Three types of sensory neurons were described based

on these parameters: C-fibers, rapidly adapting stretch receptors (RARs), and slowly adapting stretch receptors (SARs). RARs and SARs both respond to lung inflation, with different adaptation rates, while only RARs respond to lung deflation. RARs have also been proposed, along with C fibers, to detect some irritants and cytokines and perhaps mediate cough responses (Coleridge and Coleridge, 2011). It is possible that there are multiple subclasses of RARs, SARs, and C fibers, and a limitation of this classification scheme is that it does not enable genetic analysis for specific functional manipulation. Here, we initiated an alternative approach to sensory neuron classification in the vagus nerve based on receptor expression.

We identified one vagal sensory neuron type that expresses the purinergic receptor P2RY1, and generated *P2ry1-ires-Cre* mice to enable genetic access for anatomical mapping, physiological characterization, and remote control of neural activity. P2ry1 neurons innervate the lung with characteristic candelabra terminals that account for most or all vagal innervation of neuroepithelial bodies, poorly understood clusters of pulmonary endocrine cells. Ascending axons of P2ry1 neurons cross the jugular foramina and display highly regionalized and stereotyped inputs to the lateral NTS, which contains the dorsal respiratory group, a brainstem nucleus that regulates breathing (Saether et al., 1987; Speck and Feldman, 1982). Channelrhodopsin-assisted conduction velocity measurements showed that P2ry1 neurons are mostly fast-conducting A fibers, consistent with the observation that vagal sensory neurons innervating neuroepithelial bodies are myelinated (Brouns et al., 2009). Furthermore, P2ry1 neurons are capsaicin-insensitive and do not express TRPV1, but instead many express the mechanoreceptor Piezo2. Optogenetic activation of P2ry1 neurons caused an acute and dramatic pause in breathing, trapping animals in a state of exhalation. The Hering-Breuer inflation reflex, first reported in 1868, is a vagally mediated respiratory reflex evoked by pulmonary stretch-detecting SARs that innervate the lateral NTS and cause an inhibition of inspiration (Schelegle and Green, 2001). However, the Hering-Breuer inflation reflex also evokes a mild tachycardia that we did not observe following activation of P2ry1 neurons. Furthermore, pulmonary stretch receptors are thought to reside in the smooth muscle, whereas P2ry1 neurons innervate neuroepithelial bodies. An alternative possibility is that P2ry1 neurons represent a different type of A fiber distinct from RARs and SARs; the recent proposal of an A fiber nociceptor termed HTARs (Yu et al., 2007) supports the possibility of additional A fiber types and highlights the need for better cell classification schemes.

A second class of vagal sensory neuron is defined by expression of NPY2R, and *Npy2r-ires-Cre* mice were likewise generated. Npy2r neurons display enriched innervation of the alveoli-containing respiratory zone of the lung and do not contact neuroepithelial bodies. Npy2r neurons are largely slow-conducting C fibers, express the capsaicin receptor TRPV1, and respond to capsaicin in single neuron imaging experiments involving acute cultures of nodose/jugular ganglia. Centrally, Npy2r neurons target a medial posterior region of the NTS that receives pulmonary C fiber input (Kubin et al., 1991), and this region is distinct from the innervation zone of P2ry1 neurons. Optogenetic activation of Npy2r neurons caused rapid and shallow breathing, a respiratory effect reminiscent of certain pulmonary defense responses (Coleridge and Coleridge, 2011). Rapid and shallow breathing is a classical response evoked by several C fiber-activating stimuli, including bradykinin, histamine, capsaicin, irritants, and pulmonary congestion (Coleridge and Coleridge, 2011; Coleridge et al., 1983). Based on these findings, lung-innervating Npy2r neurons are likely pulmonary nociceptors.

Powerful and opposing effects on respiratory physiology were evoked by activating only a few hundred P2ry1 or Npy2r neurons in the sensory vagus nerve. Based on evidence presented here, these genetic markers label fundamentally different neuron types within the context of the respiratory system. It is possible that these neuron classes can be further subdivided into even smaller neuron groups with more specific organ targets and functions. Additional studies involving other Cre driver lines and perhaps more complex approaches such as intersectional genetics may help further delineate functionally relevant neuron types (Dymecki and Kim, 2007). P2ry1 and Npy2r sensory neurons innervate the lung as well as other tissues, but their brainstem projections are nevertheless strikingly distinct. It is possible that Cre-expressing afferents from other physiological systems influence respiratory responses. In this scenario, a prime candidate would be fibers from the cardiovascular system. However, in P2ry1 mice, a role for cardiovascular fibers seems unlikely, as activating P2ry1 neurons did not impact heart rate, as would be expected for known cardiac, aortic body, and carotid body reflexes. Furthermore, carotid body chemoreceptors promote rather than inhibit inspiration and gut fibers seem unlikely to impact respiration. Instead, a parsimonious interpretation is that observed effects on breathing are mediated by lung-derived afferents.

Neuron-selective optogenetic experiments revealed that vagal control of breathing could be dissociated from vagal control of heart rate or gastric pressure. These findings indicate that the vagus nerve contains co-fasciculating labeled lines that control specific aspects of autonomic physiology. The existence of dedicated channels in the vagus nerve for particular autonomic functions provides a streamlined flow of information that is similar to coding strategies used in other sensory systems. For example, in the gustatory system, different sensory neurons are devoted to detecting chemicals that evoke sweet, salty, sour, savory, and bitter sensations (Barretto et al., 2015; Hellekant et al., 1998). Likewise the somatosensory system contains a diversity of sensory neuron types, including those that detect gentle touch or pain (Abraira and Ginty, 2013; Basbaum et al., 2009). Here, the selective effects of P2ry1 neuron activation and the differential effects of Npy2r neuron activation indicate that functional segregation of vagal inputs can likewise begin in the periphery and persist in the brainstem, ultimately resulting in specific physiological responses.

Obtaining genetic access to sensory neurons has provided a framework for studying a myriad of perceptions, from our external senses of smell, touch, taste, vision, and hearing to internal senses associated with hunger and satiety. For example, two intermingled classes of hypothalamic neurons exert opposing effects on hunger and identifying neuropeptide markers for these neurons provided a critical basis for studying the neural control of feeding (Elmquist et al., 1999). Here, we gain genetic access to two populations of breathing control-neurons, providing a

molecular and cellular framework for understanding respiration control by the autonomic nervous system.

EXPERIMENTAL PROCEDURES

Animals
All animal procedures complied with institutional animal care and use committee guidelines. *P2ry1-ires-Cre*, *Npy2r-ires-Cre*, and *Gpr65-ires-Cre* were prepared using standard bacterial artificial chromosome (BAC) recombineering approaches (Figure S1), as previously described (Krashes et al., 2014) (see Extended Experimental Procedures). *Chat-ires-Cre* (006410), *Chat-GFP* (007902), *lox-ChR2* (012569), and *lox-tdTomato* (007914) were purchased (Jackson). *Vglut2-ires-Cre* and *lox-L10-GFP* mice (Krashes et al., 2014; Vong et al., 2011) were generous gifts from Bradford Lowell (Beth Israel Deaconess Medical Center). All Cre driver lines used are viable and fertile and abnormal phenotypes were not detected.

Receptor Expression Studies
GPCRs were identified in the nodose/jugular complex using techniques established for identifying olfactory receptors (Liberles and Buck, 2006; Liberles et al., 2009). cDNA was prepared from acutely isolated and DNase-treated nodose/jugular RNA and used as a template in qPCR reactions involving primers that recognize ∼400 endo-GPCRs (Table S1). In situ hybridization studies were performed on 10 μm cryosections of nodose/jugular ganglia as previously described (Ferrero et al., 2013; Liberles et al., 2009), except data in Figures S1 and S4C involved digoxigenin probes alternatively visualized with peroxidase conjugated anti-digoxigenin antibody and TSA-Plus-Cy5 (Perkin Elmer). Probes are described in Extended Experimental Procedures.

AAV Infections of the Nodose/Jugular Complex
The left nodose/jugular complex of adult mice was surgically exposed under anesthesia by making an incision along the ventral surface of the neck and blunt dissection. A micropipette containing a 1:1 mixture of *AAV-flex-tdTomato* (Penn Vector Core, AV-9-ALL864, titer, 1.3×10^{13} genome copies/ml), and *AAV-eGFP* (Penn Vector Core, AV-9-PV1963, titer: 3.6×10^{13} genome copies/ml), as well as 0.05% Fast Green FCF (Sigma-Aldrich) was inserted into the nodose/jugular complex. Virus solution was injected (140 nl) using a Nanoject II injector (Drummond), and success determined by Fast Green Dye filling of the ganglia. Animals recovered from surgery and were sacrificed 4 weeks later for tissue harvest.

Optogenetic Stimulation of the Vagus Nerve and Physiological Measurements
Animals were deeply anesthetized (isoflurane, 1.5%–2%, Abbott Laboratory), freely breathing, and maintained at normal body temperature. The left nodose/jugular complex was surgically exposed and an optic fiber (200 μm core, Thorlabs) coupled to a DPSS laser light source (473 nm, 150 mW, Ultralaser) positioned for focal illumination beneath the ganglion and above the pharyngeal and superior laryngeal branches. Light stimulation (5 ms pulses, 75–125 mW/mm^2 intensity, for respiratory and cardiovascular effects, 50 Hz, 10 s; for gastric pressure measurements, 5 Hz, 3–6 min) was controlled by a shutter system (Uniblitz). Respiration rate was measured using an amplifier-coupled pressure transducer (Biopac) cannulated into the trachea. A breath was scored if lung volume increased to at least 10% of mean tidal volume. Tidal volume was calculated by integrating airflow per breath, and minute volume was calculated by multiplying tidal volume by respirations per minute. Lung volume to determine state of inhalation or exhalation was determined by integrating airflow across time. Heart rhythm was measured by ECG, which was recorded with two needle electrodes placed subcutaneously on the right forepaw and the left hindpaw and amplified with a differential amplifier (A-M systems). To measure intraluminal gastric pressure, stomach contents were emptied by introducing saline through an esophageal cannula and draining through a pyloric cannula. An amplifier-coupled pressure tranducer (Biopac) was connected to a fluid-filled catheter and placed into the stomach through the pyloric sphincter. Saline (400 μL) was introduced through the esophageal cannula, and pressure measurements were acquired (1 kHz sampling, MP150

data acquisition system, Biopac). Data analyzed in 5 s bins (Figures 4C, 6B, S5A, and S5C) were normalized by comparison to values obtained during a 30 s baseline period.

Electrophysiology
For whole nerve electrophysiology, the vagus nerve was cervically transected, and the peripheral transected end was desheathed and placed onto a pair of platinum-iridium electrodes (A-M systems). Optical fibers were positioned distally to illuminate the peripheral trunk, a ground electrode was placed on nearby muscle, and the neck cavity was filled with halocarbon oil. Nerve activities were detected with an audio monitor (Grass), recorded with an alternating current (AC) preamplifier (Grass, at 1 kHz sampling rate unless specifically mentioned), and acquired on a MP150 data acquisition system (Biopac). Compound action potentials in response to a 0.8 ms light stimulus were recorded (50 kHz sampling). Fiber conduction velocity was determined by varying the distance between the optic fiber and recording electrode (travel distance); resulting time lags in peak maxima (Δt) were graphed as a function of travel distance, revealing characteristic A and C fiber types. The ratio of A to C fibers was calculated by integrating corresponding peak area in the compound action potential. Since the A and C peaks were not completely separated in most recordings, the A/C ratio reported is an underrepresentation of fold enrichment.

Data Analysis
Sample sizes are indicated in bar graphs (numbers in parenthesis), and significance was determined by comparisons to the indicated control group using a two-tailed Student's t test.

SUPPLEMENTAL INFORMATION

Supplemental Information includes Extended Experimental Procedures, seven figures, and one table and can be found with this article online at http://dx.doi.org/10.1016/j.cell.2015.03.022.

REFERENCES

Abraira, V.E., and Ginty, D.D. (2013). The sensory neurons of touch. Neuron *79*, 618–639.

Altschuler, S.M., Bao, X.M., Bieger, D., Hopkins, D.A., and Miselis, R.R. (1989). Viscerotopic representation of the upper alimentary tract in the rat: sensory ganglia and nuclei of the solitary and spinal trigeminal tracts. J. Comp. Neurol. *283*, 248–268.

Andresen, M.C., Fawley, J.A., and Hofmann, M.E. (2012). Peptide and lipid modulation of glutamatergic afferent synaptic transmission in the solitary tract nucleus. Front. Neurosci. *6*, 191.

Bailey, T.W., Hermes, S.M., Andresen, M.C., and Aicher, S.A. (2006). Cranial visceral afferent pathways through the nucleus of the solitary tract to caudal ventrolateral medulla or paraventricular hypothalamus: target-specific synaptic reliability and convergence patterns. J. Neurosci. *26*, 11893–11902.

Barretto, R.P., Gillis-Smith, S., Chandrashekar, J., Yarmolinsky, D.A., Schnitzer, M.J., Ryba, N.J., and Zuker, C.S. (2015). The neural representation of taste quality at the periphery. Nature *517*, 373–376.

Basbaum, A.I., Bautista, D.M., Scherrer, G., and Julius, D. (2009). Cellular and molecular mechanisms of pain. Cell *139*, 267–284.

Berthoud, H.R., and Neuhuber, W.L. (2000). Functional and chemical anatomy of the afferent vagal system. Auton. Neurosci. *85*, 1–17.

Brouns, I., Oztay, F., Pintelon, I., De Proost, I., Lembrechts, R., Timmermans, J.P., and Adriaensen, D. (2009). Neurochemical pattern of the complex innervation of neuroepithelial bodies in mouse lungs. Histochem. Cell Biol. *131*, 55–74.

Canning, B.J., Mori, N., and Mazzone, S.B. (2006). Vagal afferent nerves regulating the cough reflex. Respir. Physiol. Neurobiol. *152*, 223–242.

Carr, M.J., and Undem, B.J. (2003). Bronchopulmonary afferent nerves. Respirology *8*, 291–301.

Coleridge, H.M., and Coleridge, J.C. (2011). Reflexes evoked from tracheobronchial tree and lungs. Compr. Physiol. 395–429.

Coleridge, H.M., Coleridge, J.C., and Roberts, A.M. (1983). Rapid shallow breathing evoked by selective stimulation of airway C fibres in dogs. J. Physiol. *340*, 415–433.

Coste, B., Mathur, J., Schmidt, M., Earley, T.J., Ranade, S., Petrus, M.J., Dubin, A.E., and Patapoutian, A. (2010). Piezo1 and Piezo2 are essential components of distinct mechanically activated cation channels. Science *330*, 55–60.

Dong, X., Han, S., Zylka, M.J., Simon, M.I., and Anderson, D.J. (2001). A diverse family of GPCRs expressed in specific subsets of nociceptive sensory neurons. Cell *106*, 619–632.

Dymecki, S.M., and Kim, J.C. (2007). Molecular neuroanatomy's "Three Gs": a primer. Neuron *54*, 17–34.

Elmquist, J.K., Elias, C.F., and Saper, C.B. (1999). From lesions to leptin: hypothalamic control of food intake and body weight. Neuron *22*, 221–232.

Ferrero, D.M., Moeller, L.M., Osakada, T., Horio, N., Li, Q., Roy, D.S., Cichy, A., Spehr, M., Touhara, K., and Liberles, S.D. (2013). A juvenile mouse pheromone inhibits sexual behaviour through the vomeronasal system. Nature *502*, 368–371.

Foley, J.O., and DuBois, F.S. (1937). Quantitative studies of the vagus nerve in the cat. J. Comp. Neurol. *67*, 49–67.

Fox, E.A., Phillips, R.J., Baronowsky, E.A., Byerly, M.S., Jones, S., and Powley, T.L. (2001). Neurotrophin-4 deficient mice have a loss of vagal intraganglionic mechanoreceptors from the small intestine and a disruption of short-term satiety. J. Neurosci. *21*, 8602–8615.

Gonzalez, C., Almaraz, L., Obeso, A., and Rigual, R. (1994). Carotid body chemoreceptors: from natural stimuli to sensory discharges. Physiol. Rev. *74*, 829–898.

Groves, D.A., and Brown, V.J. (2005). Vagal nerve stimulation: a review of its applications and potential mechanisms that mediate its clinical effects. Neurosci. Biobehav. Rev. *29*, 493–500.

Guyenet, P.G., Stornetta, R.L., and Bayliss, D.A. (2010). Central respiratory chemoreception. J. Comp. Neurol. *518*, 3883–3906.

Hellekant, G., Ninomiya, Y., and Danilova, V. (1998). Taste in chimpanzees. III: Labeled-line coding in sweet taste. Physiol. Behav. *65*, 191–200.

Kalia, M., and Mesulam, M.M. (1980). Brain stem projections of sensory and motor components of the vagus complex in the cat: II. Laryngeal, tracheobronchial, pulmonary, cardiac, and gastrointestinal branches. J. Comp. Neurol. *193*, 467–508.

Karra, E., and Batterham, R.L. (2010). The role of gut hormones in the regulation of body weight and energy homeostasis. Mol. Cell. Endocrinol. *316*, 120–128.

Katz, D.M., and Karten, H.J. (1983). Visceral representation within the nucleus of the tractus solitarius in the pigeon, Columba livia. J. Comp. Neurol. *218*, 42–73.

Kim, D.G., Kang, H.M., Jang, S.K., and Shin, H.S. (1992). Construction of a bifunctional mRNA in the mouse by using the internal ribosomal entry site of the encephalomyocarditis virus. Mol. Cell. Biol. *12*, 3636–3643.

Krashes, M.J., Shah, B.P., Madara, J.C., Olson, D.P., Strochlic, D.E., Garfield, A.S., Vong, L., Pei, H., Watabe-Uchida, M., Uchida, N., et al. (2014). An excitatory paraventricular nucleus to AgRP neuron circuit that drives hunger. Nature *507*, 238–242.

Kubin, L., Kimura, H., and Davies, R.O. (1991). The medullary projections of afferent bronchopulmonary C fibres in the cat as shown by antidromic mapping. J. Physiol. *435*, 207–228.

Kubin, L., Alheid, G.F., Zuperku, E.J., and McCrimmon, D.R. (2006). Central pathways of pulmonary and lower airway vagal afferents. J. Appl. Physiol. *101*, 618–627.

Liberles, S.D., and Buck, L.B. (2006). A second class of chemosensory receptors in the olfactory epithelium. Nature *442*, 645–650.

Liberles, S.D., Horowitz, L.F., Kuang, D., Contos, J.J., Wilson, K.L., Siltberg-Liberles, J., Liberles, D.A., and Buck, L.B. (2009). Formyl peptide receptors are candidate chemosensory receptors in the vomeronasal organ. Proc. Natl. Acad. Sci. USA *106*, 9842–9847.

Munger, S.D., Leinders-Zufall, T., and Zufall, F. (2009). Subsystem organization of the mammalian sense of smell. Annu. Rev. Physiol. *71*, 115–140.

Paintal, A.S. (1973). Vagal sensory receptors and their reflex effects. Physiol. Rev. *53*, 159–227.

Rogan, S.C., and Roth, B.L. (2011). Remote control of neuronal signaling. Pharmacol. Rev. *63*, 291–315.

Rossi, J., Balthasar, N., Olson, D., Scott, M., Berglund, E., Lee, C.E., Choi, M.J., Lauzon, D., Lowell, B.B., and Elmquist, J.K. (2011). Melanocortin-4 receptors expressed by cholinergic neurons regulate energy balance and glucose homeostasis. Cell Metab. *13*, 195–204.

Saether, K., Hilaire, G., and Monteau, R. (1987). Dorsal and ventral respiratory groups of neurons in the medulla of the rat. Brain Res. *419*, 87–96.

Schachter, S.C., and Saper, C.B. (1998). Vagus nerve stimulation. Epilepsia *39*, 677–686.

Schelegle, E.S., and Green, J.F. (2001). An overview of the anatomy and physiology of slowly adapting pulmonary stretch receptors. Respir. Physiol. *125*, 17–31.

Schmidt-Supprian, M., and Rajewsky, K. (2007). Vagaries of conditional gene targeting. Nat. Immunol. *8*, 665–668.

Speck, D.F., and Feldman, J.L. (1982). The effects of microstimulation and microlesions in the ventral and dorsal respiratory groups in medulla of cat. J. Neurosci. *2*, 744–757.

Tränkner, D., Hahne, N., Sugino, K., Hoon, M.A., and Zuker, C. (2014). Population of sensory neurons essential for asthmatic hyperreactivity of inflamed airways. Proc. Natl. Acad. Sci. USA *111*, 11515–11520.

Vong, L., Ye, C., Yang, Z., Choi, B., Chua, S., Jr., and Lowell, B.B. (2011). Leptin action on GABAergic neurons prevents obesity and reduces inhibitory tone to POMC neurons. Neuron *71*, 142–154.

Widdicombe, J. (2001). Airway receptors. Respir. Physiol. *125*, 3–15.

Yarmolinsky, D.A., Zuker, C.S., and Ryba, N.J. (2009). Common sense about taste: from mammals to insects. Cell *139*, 234–244.

Yu, J., Lin, S., Zhang, J., Otmishi, P., and Guardiola, J.J. (2007). Airway nociceptors activated by pro-inflammatory cytokines. Respir. Physiol. Neurobiol. *156*, 116–119.

EXTENDED EXPERIMENTAL PROCEDURES

Generation of Gene Targeted Mice

A vector was designed to contain the *ires-Cre* cassette, an excisable neomycin resistance gene, and homology arms for cassette insertion 3 base pairs downstream of the receptor stop codon. Vectors were electroporated into W4/129S6 ES cells and selected for neomycin resistance. Appropriately targeted cells were identified by Southern Blot and PCR analysis, and injected into C57/BL6 blastocysts to generate chimeric animals. The neomycin resistance gene was subsequently removed by crossing with *Act-Flpe* (Jackson, 003800).

PCR Primers for Mouse Genotyping

Animals were genotyped with primers that target the 'ires-cre' insertion (primers used: *P2ry1* WT allele: TCCTGACGGTGTTT GCTGTG and AGGTTCAAGTTCCAGGTGGC; *P2ry1* TG allele: TCCTGACGGTGTTTGCTGTG and GACATTCAACAGACCTTGCA TTCC; *Npy2r* WT allele: CAAGCATCGGTAATCAGAACG and ACTCATCTTCACCGTGTTCCAC; *Npy2r* TG allele: GCCCTGGAAGG GATTTTTGAAGCA and ATGGCTAATCGCCATCTTCCAGCAA;
   Gpr65 WT allele: GGAGAGCTGATATGTGGAAC and CCAGTACATGGAGTGGCTTC;
   Gpr65 TG allele: CCTGTTTCGGACGTGCATGG and GGAGGGAGAGGGGCGGAATT).

Southern Blot Analysis

Southern blot analysis involved standard protocols. 5′ and 3′ probes (500 bp, amplified by PCR from mouse genomic DNA using primers described below, Figure S2) were radioactively labeled with dCTP [α-^{33}P] (PerkinElmer) using a DNA labeling system (GE Healthcare) and purified with NickTM columes (GE Healthcare). Primers to make probes: *P2ry1* 5′ probe: TTAGCAAAGACAAAG CAGGC and AAACCAGCTCTGACAAAGTGAC; *P2ry1* 3′ probe: AAACCTCAGTTCTGAACACAAGGCTGC and AGGCCAGTAGG CACTTCCTATGAATATGC; *Npy2r* 5′ probe: TTCCAGTGATTTCAGCATGTAGTTAAAGCAGGAG and ACATTTTCTTCCCTCTGAA ATCCTTTCGCTG; *Npy2r* 3′ probe: TGCTTTCATCTAAAATGATTGATAAGTGATCTTTCC and AAATCCTCAAGTTGAGCCTTAGCC CAATTTC. 10 μg ES cell genomic DNA was digested (overnight, 37°C) with restriction enzymes (HpaI for *Npy2r-ires-cre*, expected sizes: WT 15.5 kb, 5′ TG 10.8 kb, 3′ TG 8.8 kb; BamHI for *P2ry1-ires-cre*, expected sizes: WT 17.0 kb, 5′ TG 9.5 kb, 3′ TG 8.5 kb).

Probes for RNA In Situ Hybridization

Digoxigenin or Fluorescein-labeled cRNA riboprobes were used for *P2ry1* (full coding sequence, 1122 bp), *Npy2r* (full coding sequence, 1146 bp), *Gpr65* (full coding sequence, 1014 bp), *Piezo2* (1112 bp amplified by primers ACATGGGTTCTGTTCCTG and ATCATCCAGAAGCGTCGG), *Trpv1* (500 bp amplified by primers ATGGAGAAATGGGCTAGCTTAGACT and TGCAGATTGAG CATGGCTTTGAGCA), *eGFP/eYFP* (545 bp amplified by primers AGCTGACCCTGAAGTTCATCTG and CTCCAGCAGGACCATGT GAT) and *tdTomato* (615 bp amplified by primers ATCAAAGAGTTCATGCGCTTC and GTTCCACGATGGTGTAGTCCTC).

Visualization of Sensory Neuron Fibers and Cell Bodies

Tissues (lung, brain, nodose/jugular ganglia) were collected for fluorescence imaging (unfixed) and immunohistochemistry (fixed). Whole mount analysis of native (reporter-derived) tissue fluorescence in immobilized nodose/jugular ganglia was imaged by confocal microscopy (Leica SP5 II, maximum projections of confocal stacks), and in a flattened lung lobe was imaged using an Olympus VS120 whole slide scanner. For immunohistochemistry, fixation involved standard protocols for transcardial perfusion with paraformaldehyde, post-dissection fixation and sucrose cryopreservation (Ferrero et al., 2013). Immunohistochemistry was performed on tissue cryosections (lung: 50 μm, brain: 25 μm, nodose ganglion: 10 μm) using standard techniques involving Chicken-anti-GFP (Abcam, AB_300798, 1:1000), Rabbit-anti-DsRed (Clontech, AB_10013483, 1:1000), Rabbit-anti-CGRP (Sigma, AB_259091, 1:10,000), Donkey-anti-Chicken-647 (Jackson ImmunoResearch, AB_2340379, 1:300), Donkey-anti-Chicken-488 (Jackson ImmunoResearch, AB_2340375, 1:300), Donkey-anti-Rabbit-Cy3 (Jackson ImmunoResearch, AB_2307443, 1:300) and Donkey-anti-Rabbit-647 (Jackson ImmunoResearch, AB_2340624, 1:300) antibodies. Widefield and confocal fluorescent images of brain and lung sections were captured on Leica SP5 II and Nikon Ti Inverted Fluorescence microscopes. In Figure 1C, native L10-GFP fluorescence was imaged in fixed tissue and counterstained with a red fluorescent Nissl stain (NeuroTrace 530/615, Invitrogen, 1:300).

   For quantitative analysis of lung and brainstem innervation, we counted the number of fluorescent pixels, which we defined as pixels with a fluorescence intensity greater than maximum off-tissue background fluorescence. Counts were obtained for both tdTomato (T) and GFP (G) to generate the T/G ratio described in Figures 2 and 7. In each lung section, a 17.5-mm^2 region was selected from similar locations that contained large airways and dense GFP-immunolabeling. Three lung sections were measured per animal (n = 2). In brainstem sections, similar numbers of GFP fluorescent pixels were revealed following infection of *P2ry1-ires-Cre* (L-NTS: 82169, M-NTS: 251864, AP: 36652) and *Npy2r-ires-Cre* mice (L-NTS: 74035, M-NTS: 253239, AP: 22121). To quantify innervation of neuroepithelial bodies and alveoli, we examined fluorescence from tdTomato (native), GFP (immunofluorescence), and CGRP (immunofluorescence). Neuroepithelial bodies innervated by tdTomato and/or GFP fibers were counted, and data are expressed as the number of tdTomato-innervating neuroepithelial bodies per 100 GFP-innervating neuroepithelial bodies per mouse (n = 3 - 5). In *Vglut2-ires-Cre* animals, more neuroepithelial bodies were innervated by fibers visualized with GFP than tdTomato, due to the

enhanced sensitivity of immunofluorescence. Alveolar fibers were defined as an arborizing fiber located at least 50 μm from a large airway, and counts were similarly normalized to 100 GFP terminals (n = 5).

In Vitro Calcium Imaging of Acutely Dissociated Vagal Sensory Neurons

Left and right nodose/jugular ganglia were harvested from *Vglut2-ires-cre*; *lox-tdTomato*, *P2ry1-ires-cre*; *lox-L10-GFP*, and *Npy2r-ires-cre*; *lox-L10-GFP* animals. Ganglia were digested with enzyme mix (collagenase I (1 mg/ml, Roche), Dispase II (3 mg/ml, Roche)) at 37°C for 40-45 min, washed with L-15 medium (Invitrogen), and gently triturated with three glass aspiration pipettes of decreasing diameters. Isolated single cells were filtered with a 40 μm cell strainer (BD Falcon), resuspended in culture medium (10% FBS in L-15 medium), placed onto laminin-coated cover glass and incubated ∼2 hr at 37°C until most cells were attached to the glass surface. Cells were loaded with Fura-2 AM (Invitrogen) for 30 min and imaged with excitation wavelength at 340 and 380 nm for responses to capsaicin (2 μM) and KCl (150 mM, except for Figure 3, 50 mM).

Fluoro-Gold Labeling of Motor Neurons

Parasympathetic preganglionic neurons of the DMV and nucleus ambiguus were labeled in *Vglut2-ires-Cre*; *lox-L10-GFP* and *Chat-ires-Cre*; *lox-L10-GFP* mice via intraperitoneal injection of Fluoro-Gold (Fluorchrome, 30 mg/kg). Brains were harvested 5 days post-injection, sectioned, and imaged for native GFP and Fluoro-Gold fluorescence.
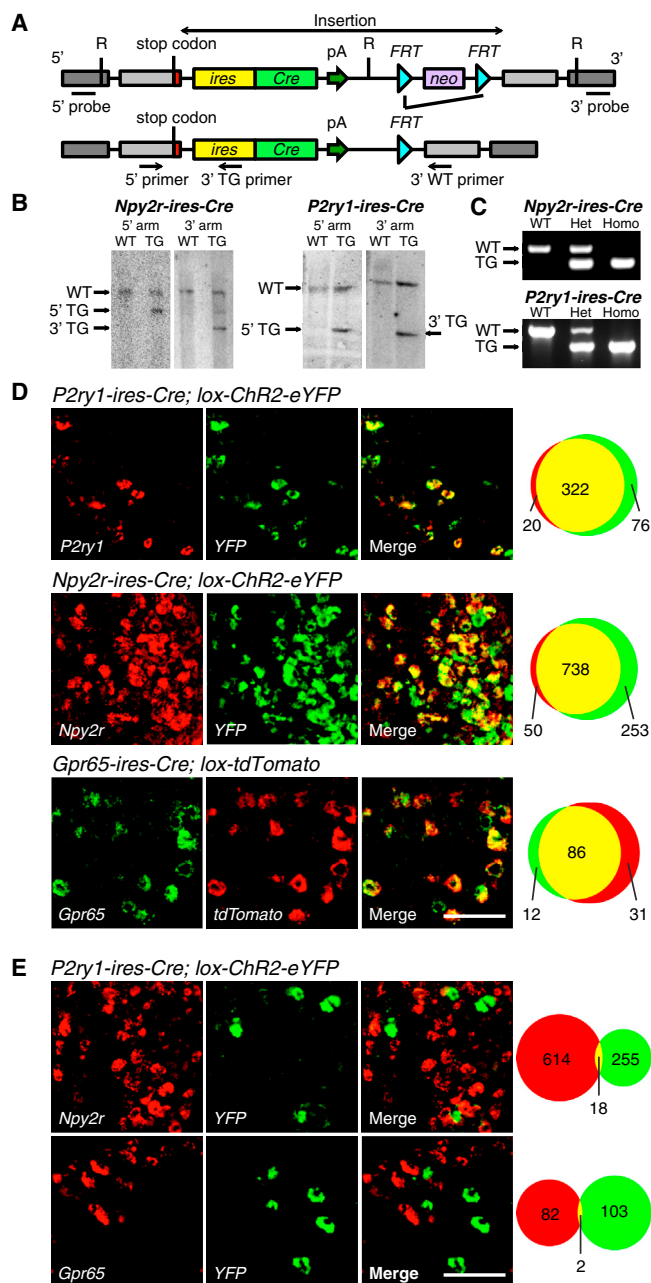
Figure S1. Construction and Validation of *P2ry1-ires-Cre*, *Npy2r-ires-Cre*, and *Gpr65-ires-Cre* Mice, Related to Figure 1

(A) Design strategy for *ires-Cre* knockin alleles. *ires-Cre* alleles were inserted after the endogenous stop codon, along with a poly A (pA) tail, and a gene encoding neomycin (neo) resistance. The neo cassette was flanked by flippase recognition target (FRT) sites which enabled excision by crossing to mice that express germline Flp recombinase. Primers, probes, and restriction (R) sites indicated were used for subsequent genotype determination.

(B) Southern blot analysis of genomic DNA from wild-type (WT) or knockin ES cells (TG).

(C) PCR analysis of genomic DNA from mice indicated using primers that recognize the wild-type (WT) or knockin (TG) alleles.

(D and E) Two color RNA in situ hybridization experiments in the nodose/jugular complex with animal genotypes and RNA riboprobes indicated. The numbers of cells expressing each gene alone (green, red) or together (yellow) were counted. Scale bars, 100 μm.
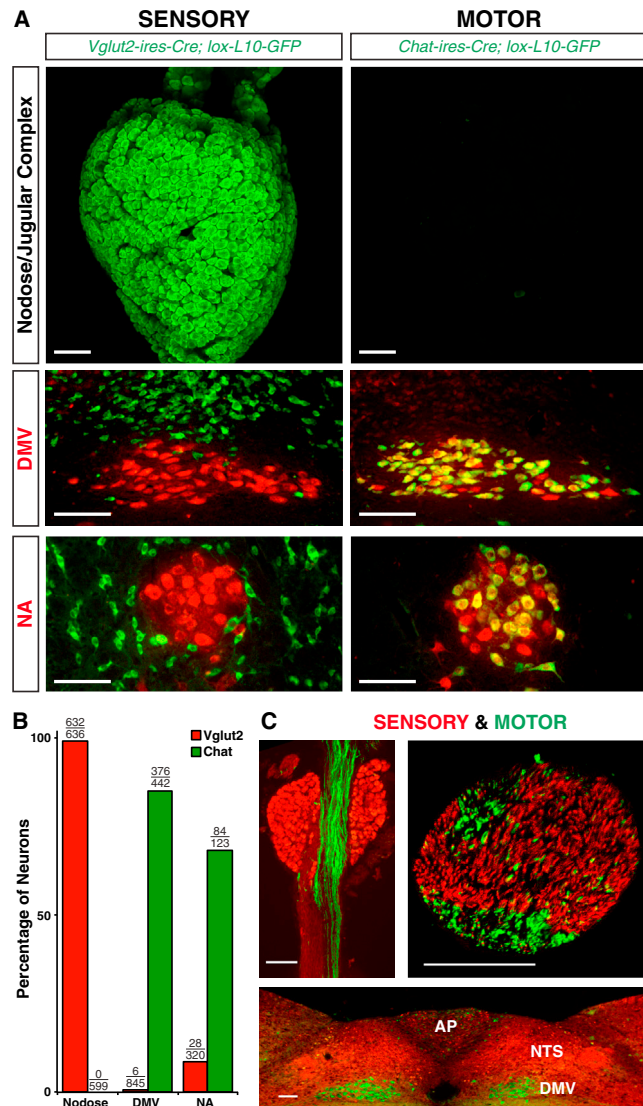
Figure S2. Vglut2 and Chat Provide Largely Selective Markers for Sensory and Motor Arms of the Vagus Nerve, Related to Figure 1

(A) Native fluorescence in whole mount analysis of nodose/jugular complex (top) or in brainstem cryosections containing the DMV and nucleus ambiguus (NA) of mice indicated. Motor cell bodies were labeled by intraperitoneal injection of Fluoro-Gold (red). Scale bars, 100 μm.

(B) Numbers of sensory and motor cell bodies labeled by *Vglut2-ires-Cre; lox-L10-GFP* and *Chat-ires-Cre; lox-L10-GFP* drivers. Neuron counts are expressed as a percentage of Nissl stained sensory neurons or Fluoro-Gold labeled motor neurons.

(C) Fluorescence microscopy images of the nodose/jugular complex (top left), a transverse section of the cervical vagus nerve trunk (top right), and a region of the brainstem from *Vglut2-ires-Cre; lox-tdTomato; Chat-eGFP* mice. Scale bars, 100 μm.
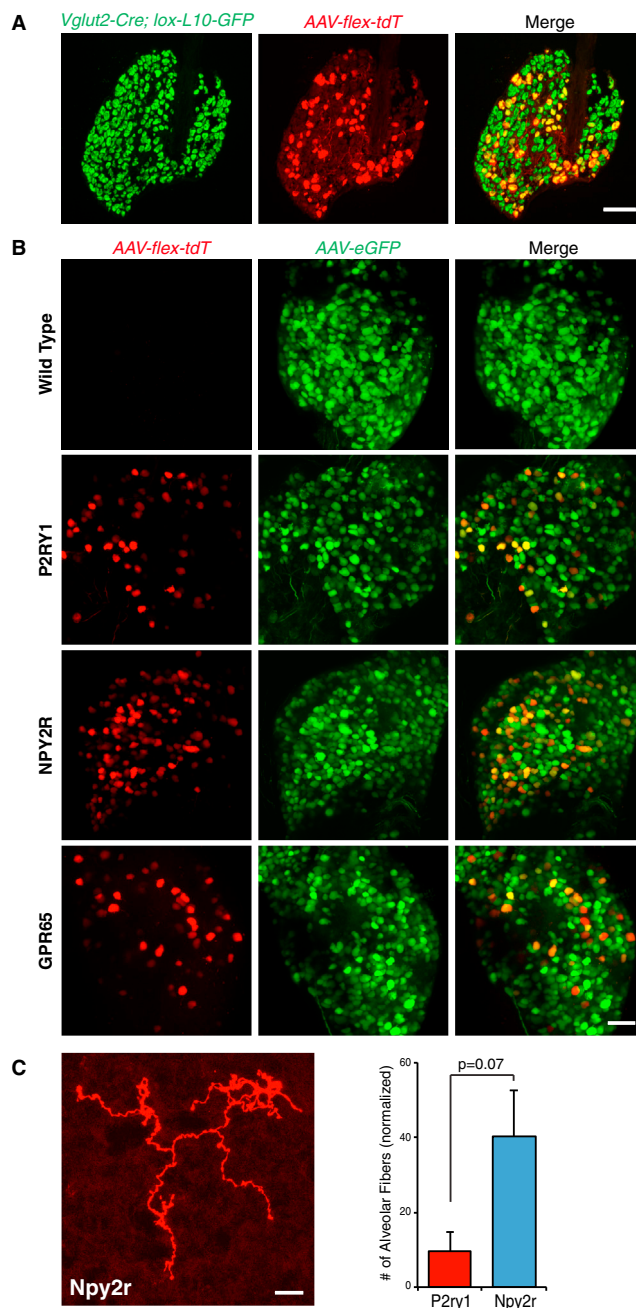
Figure S3. AAV-Assisted Visualization of Sensory Neurons in the Nodose/Jugular Complex and Lung Respiratory Zone, Related to Figure 2

(A) Infection efficiency was determined by infecting AAV-flex-tdTomato (tdT) in the nodose/jugular complex of *Vglut2-ires-Cre; lox-L10-GFP*. (Cryosection, native fluorescence; scale bars, 100 μm).

(B) Cre-dependent AAVs similarly infect vagal sensory neurons in *P2ry1-ires-Cre*, *Npy2r-ires-Cre*, and *Gpr65-ires-Cre* mice, but not wild-type mice. (Whole mount, native fluorescence; scale bars, 100 μm).

(C) A representative Npy2r fiber near lung alveoli (left); counts of alveolar P2ry1 and Npy2r fibers (right), normalized to fibers visualized with *AAV-eGFP*. Scale bar, 20 μm, (n = 5, mean ± sem).
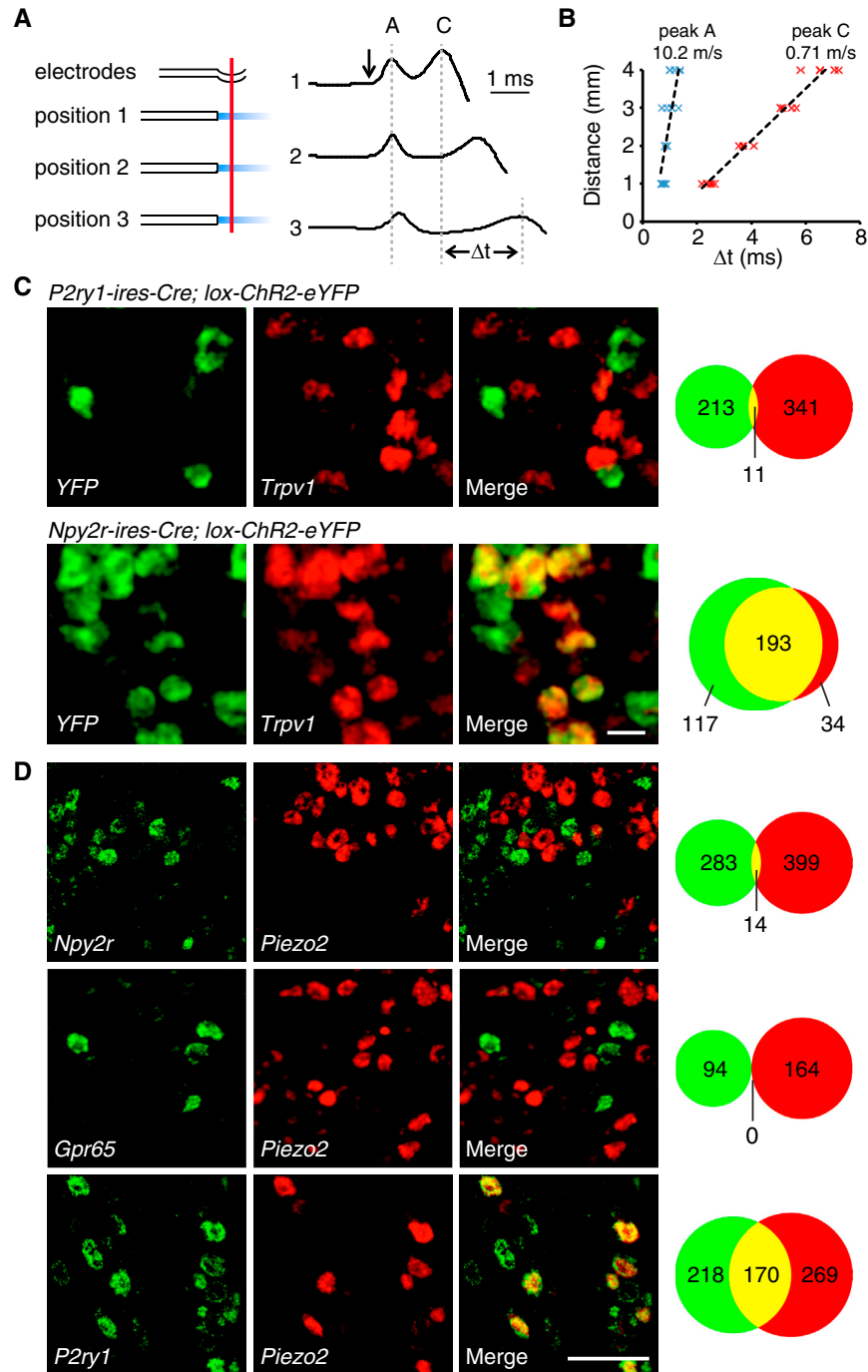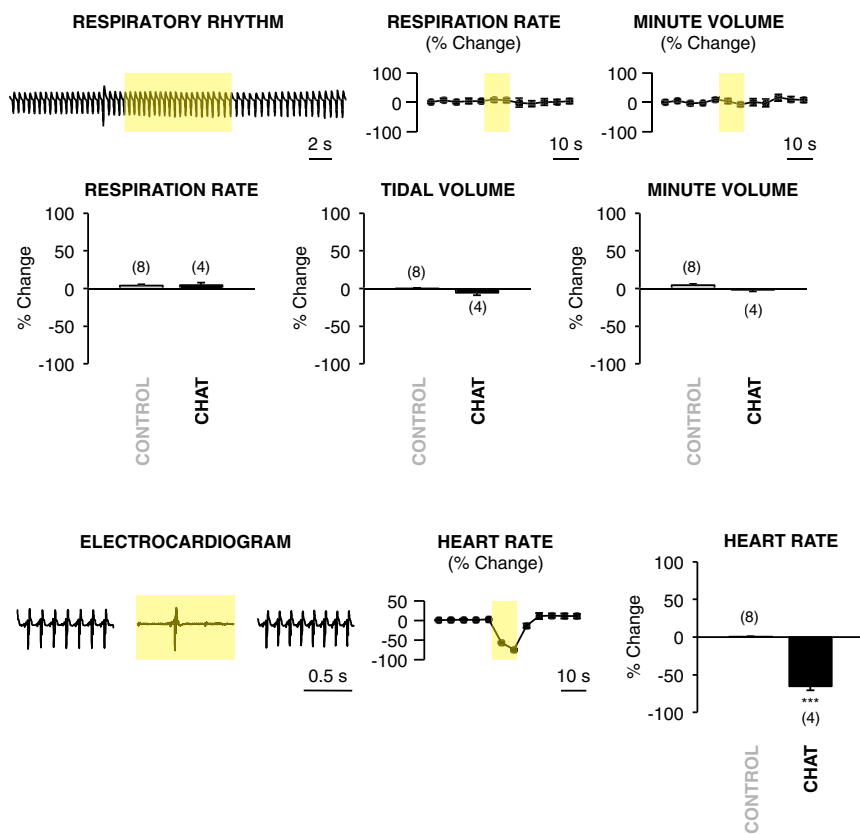
Figure S4. Electrophysiological and Molecular Characterization of P2ry1 and Npy2r Neurons, Related to Figure 3

(A) Neuron conduction velocities were measured by changing the distance between the optic fiber and recording electrodes on the vagus nerve (red line). Representative compound action potentials resulting from brief optogenetic stimulation (arrow) in *Vglut2-ires-Cre* mice, with time delays (Δt) of peak A and peak C maxima observed at distant stimulation positions.

(B) Δt is graphed as a function of distance between stimulating positions, with slope revealing peak velocities characteristic of A and C fibers.

(C and D) Two color RNA in situ hybridization experiments in the nodose/jugular complex with knockin mice (C) or wild-type mice (D) and RNA riboprobes depicted. The numbers of cells expressing each gene alone (green, red) or together (yellow) were counted. Scale bars, (C) 20 μm; (D) 100 μm.

A *Chat-ChR2*

RESPIRATORY RHYTHM

RESPIRATION RATE
(% Change)

MINUTE VOLUME
(% Change)

RESPIRATION RATE

TIDAL VOLUME

MINUTE VOLUME

ELECTROCARDIOGRAM

HEART RATE
(% Change)

HEART RATE

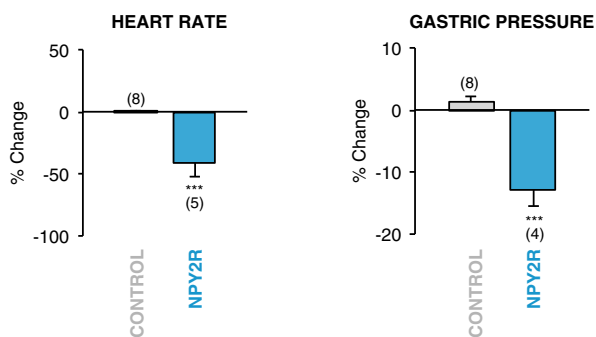**B** *Npy2r-ChR2*

HEART RATE

GASTRIC PRESSURE

Figure S5. Optogenetic Activation of Vagal Motor Fibers and Npy2r Neurons, Related to Figures 4 and 6

(A) Illumination (yellow shading) of the vagus nerve in *Chat-ChR2* mice (motor fibers) or *lox-ChR2* (control) mice does not impact respiratory rhythm, respiration rate, tidal volume, or minute volume, either in 5 s bins (top middle, top right) or across the illumination period (middle). Illumination (yellow shading) of the vagus nerve in *Chat-ChR2* mice but not control (*lox-ChR2*) mice causes a powerful decrease in heart rate (bottom).

(B) Illumination of the vagus nerve in *Npy2r-ChR2* mice lowers heart rate and gastric pressure (mean ± sem, ***p < 0.001).
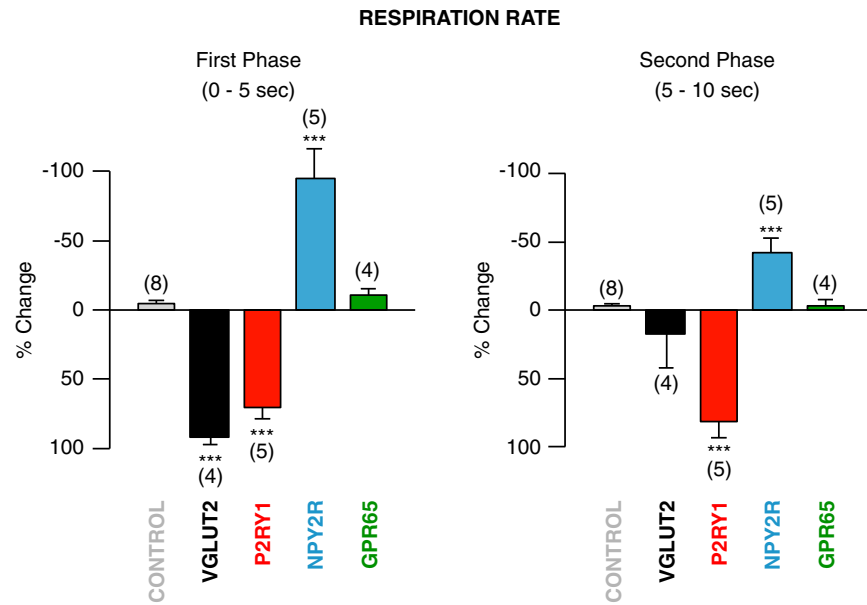
RESPIRATION RATE

Figure S6. Distinguishing Early and Late Respiratory Effects following Activation of Different Genetically Defined Vagal Sensory Neurons, Related to Figure 4

Light-induced changes in respiration rate were measured in *Vglut2-ChR2*, *P2ry1-ChR2*, *Npy2r-ChR2*, *Gpr65-ChR2*, and control (*lox-ChR2*) mice. Effects across the first five seconds (left, First Phase) and the second five seconds (right, Second Phase) were compared in each line. (mean ± sem, ***p < 0.001).
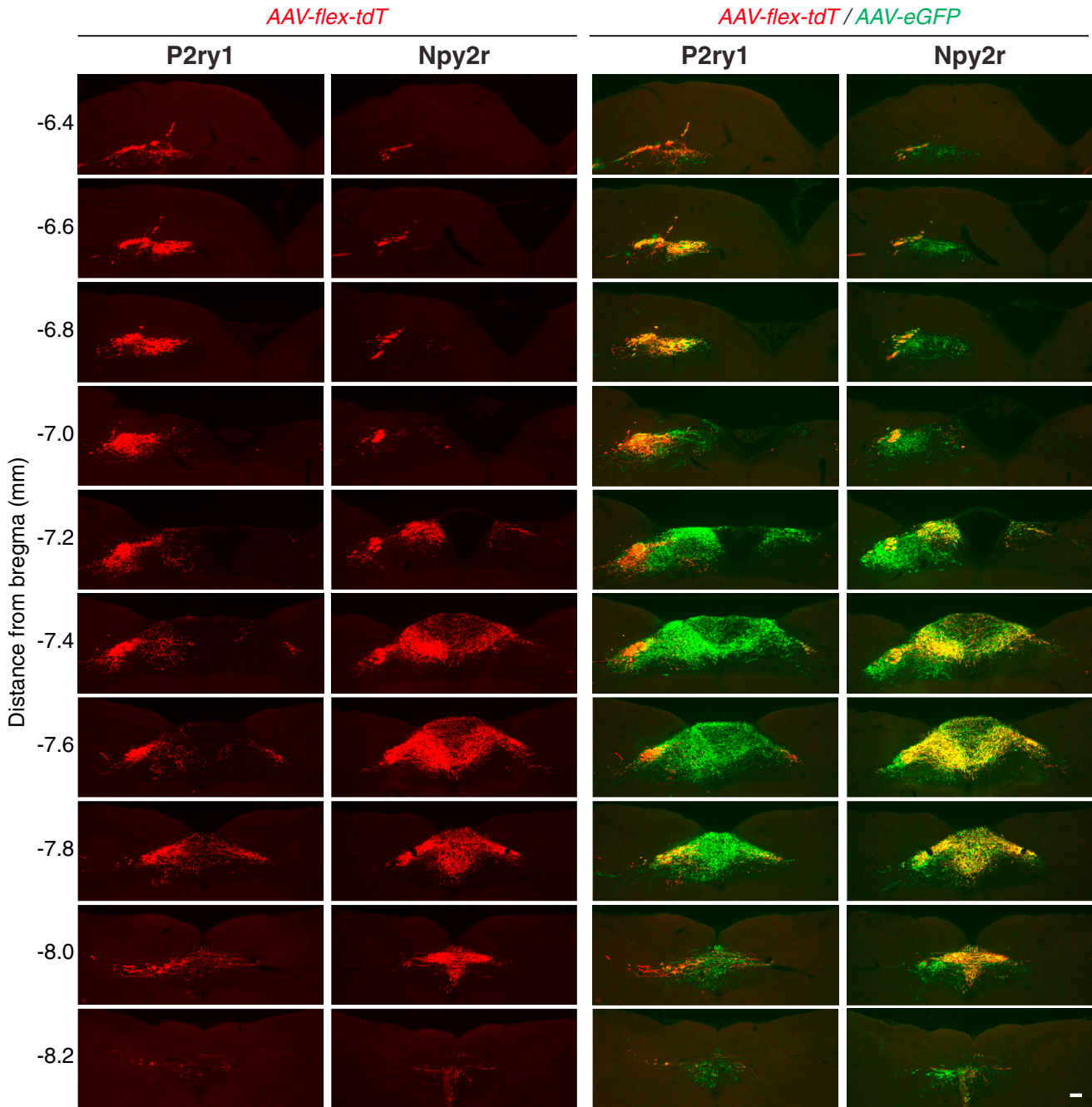
Figure S7. Central Innervation Patterns of P2ry1 and Npy2r Vagal Neurons Are Revealed across the Entire Rostral-Caudal Axis, Related to Figure 7

The nodose/jugular ganglia of *P2ry1-ires-Cre* and *Npy2r-ires-Cre* mice were infected with both AAV-flex-tdT and AAV-eGFP. Fixed brainstem cryosections were analyzed by two color immunohistochemistry for tdTomato (red) and eGFP (green) Scale bars, 100 μm.